


RESEARCH ARTICLE

Open Access



Diversely evolved xibalbin variants from remipede venom inhibit potassium channels and activate PKA-II and Erk1/2 signaling

Ernesto Lopes Pinheiro-Junior^{1†}, Ehsan Alirahimi^{2†}, Steve Peigneur¹, Jörg Isensee², Susanne Schiffmann³, Pelin Erkoc^{4,5}, Robert Fürst^{4,5}, Andreas Vilcinskas^{5,6}, Tobias Sennoner⁷, Ivan Koludarov⁷, Benjamin-Florian Hempel⁸, Jan Tytgat¹, Tim Hucho² and Björn M. von Reumont^{5,9*} 

Abstract

Background The identification of novel toxins from overlooked and taxonomically exceptional species bears potential for various pharmacological applications. The remipede *Xibalbanus tulumensis*, an underwater cave-dwelling crustacean, is the only crustacean for which a venom system has been described. Its venom contains several xibalbin peptides that have an inhibitor cysteine knot (ICK) scaffold.

Results Our screenings revealed that all tested xibalbin variants particularly inhibit potassium channels. Xib₁ and xib₁₃ with their eight-cysteine domain similar to spider knottins also inhibit voltage-gated sodium channels. No activity was noted on calcium channels. Expanding the functional testing, we demonstrate that xib₁ and xib₁₃ increase PKA-II and Erk1/2 sensitization signaling in nociceptive neurons, which may initiate pain sensitization. Our phylogenetic analysis suggests that xib₁₃ either originates from the common ancestor of pancrustaceans or earlier while xib₁ is more restricted to remipedes. The ten-cysteine scaffolded xib₂ emerged from xib₁, a result that is supported by our phylogenetic and machine learning-based analyses.

Conclusions Our functional characterization of synthesized variants of xib₁, xib₂, and xib₁₃ elucidates their potential as inhibitors of potassium channels in mammalian systems. The specific interaction of xib₂ with Kv1.6 channels, which are relevant to treating variants of epilepsy, shows potential for further studies. At higher concentrations, xib₁ and xib₁₃ activate the kinases PKA-II and ERK1/2 in mammalian sensory neurons, suggesting pain sensitization and potential applications related to pain research and therapy. While tested insect channels suggest that all probably act as neurotoxins, the biological function of xib₁, xib₂, and xib₁₃ requires further elucidation. A novel finding on their evolutionary origin is the apparent emergence of *X. tulumensis*-specific xib₂ from xib₁. Our study is an important cornerstone for future studies to untangle the origin and function of these enigmatic proteins as important components of remipede but also other pancrustacean and arthropod venoms.

[†]Ernesto Lopes Pinheiro-Junior and Ehsan Alirahimi contributed equally to this work.

*Correspondence:
Björn M. von Reumont
bmvr@reumont.net

Full list of author information is available at the end of the article



Keywords Venomous crustaceans, Marine venoms, Xibalbanus, Xibalbin₁, Xibalbin₁₃, Xibalbin₂, Electrophysiology, HCl screening, ICK, Knottin

Background

Venomous animals inject their toxic compounds into other organisms primarily for self-defense or predation [1, 2]. Numerous venoms comprise proteins that have evolved to modulate a range of physiological functions in their target organisms. Investigating these bioactivities may lead to pharmacological or agrochemical applications [1–5]. The majority of venoms and venom proteins that have been thoroughly studied mainly originate from iconic and terrestrial groups such as snakes, spiders, scorpions, and insects [2, 6–8]. Marine species have received limited research attention, with only a small number of fish and invertebrate species (such as sea anemones, jellyfish, cone snails, cephalopods, polychaetes, and recently nemerteans [6, 9–19]) being better studied. As venoms and their toxic proteins have independently evolved in various animal lineages, researching new lineages presents on the one hand an opportunity to identify novel venom compounds with interesting bioactivity and on the other hand to enhance our understanding of the evolution of convergent functional traits generally [2, 6, 20–25].

Only one venomous species of marine crustaceans has been described so far in more detail [26, 27]. *Xibalbanus tulumensis* belongs to the crustacean class Remipedia, which was first described over 40 years ago (Yager 1981) and currently comprises 28 extant species [28, 29]. However, the internal relationships of remipedes remain challenging [6, 26–28]. Phylogenomic analyses show that remipedes share a common ancestor with hexapods, making them a key taxon for comprehending insect evolution [30–34]. The biology and ecology of remipedes are not yet comprehensively understood, likely due to the extraordinary and secluded environment they inhabit as stygobionts in the marine saltwater regions of anchialine underwater cave systems [35].

The venom system of *X. tulumensis* and its anatomy has been studied using synchrotron-based μ -computer tomography in the first comprehensive publication about remipede venom [26]; see Fig. 1.

Remipedes have large thoracic glands connected to reservoirs in their second maxillules, which release venom through an apical pore under a terminal claw [36]. This venom injection is facilitated by complex muscle arrangements [26, 36], though it is worth noting that direct observations of remipedes catching prey are lacking. Transcriptomics identified putative venom components, later detailed in the first

proteo-transcriptomics study using squeezed-out gland lumen proteome [27]; see Fig. 1. Three main groups of peptides and proteins were found: enzymes, including chitinase, peptidase S1, and LDLa-domain containing peptidase S1; moderately expressed non-enzymatic proteins; and novel peptides (xibalbins). Many of these peptides resemble inhibitor cysteine knot peptides (ICKs or knottins), known for their robustness against enzymes, heat, and pH due to their characteristic cysteine scaffold that results in specific numbers of disulfide bridges [37, 38]. In various animal venoms, ICK peptides function as neurotoxins, hemolytics, or antibacterials, and they are also explored for pharmacological and agrochemical applications [3, 39].

The hypothesized mechanism of envenomation by remipedes, based on proteo-transcriptome data sequence similarities [27], suggests that xibalbin1 (xib₁), xibalbin2 (xib₂), and xibalbin13 (xib₁₃) ICK-like protein families, and the double-ICK-like xibalbin3 (xib₃), could act as putative neurotoxins that rapidly cause paralysis in prey during an attack. Simultaneously, the proteins and enzymes break down internal tissues and structures, resulting in prey liquefaction and subsequent feeding by remipedes [27]. However, it should be noted that bioactivity tests for the venom compounds of remipedes, particularly the ICK-like peptides, have been lacking so far.

In this study, we investigate the bioactivity of synthetic variants of xib₁, xib₁₃, and xib₂ focused on possible application potential, examining their cytotoxicity (including cancer cell lines), ability to modulate ion channels, and impact on sensory neurons. Our research explores also insight into their biological functions by testing insect targets. Furthermore, we shed first light on the diversity and origin of ICK-like peptides in remipedes by including sequences from further species besides *X. tulumensis* using phylogenetic and machine learning approaches.

Results

Xib₁ is unique in remipedes while xib₁₃ is similar to other ICKs, whereas xib₂ and xib₃ are specific to *Xibalbanus*

To broaden the scope of our study beyond the single species *X. tulumensis*, we examined potential variants of xib₁, xib₂, xib₁₃, and xib₃ (double ICK, not tested in this study) in four other remipedes. This analysis was based on de novo assembled transcripts from *X. tulumensis* from which secreted proteins were identified

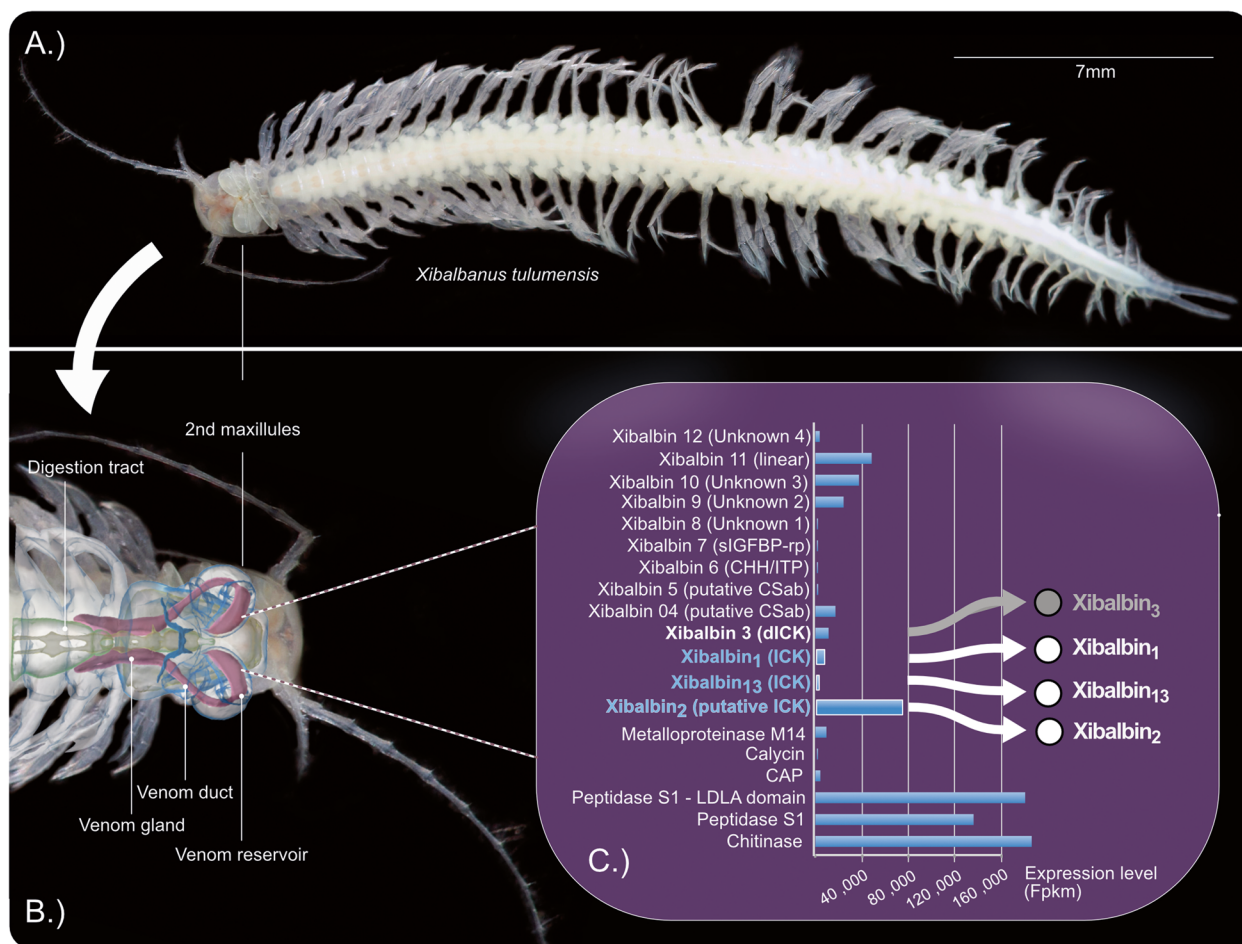


Fig. 1 Overview of published data used for our study to investigate bioactivity of the higher expressed ICK-like peptides. **A** Habitus of an adult remipede *X. tulumensis*. **B** The anatomy of the venom system as described in von Reumont et al. [26] is illustrated by blending a synchrotron-based microcomputer tomography reconstruction into a light microscope picture. All components of the venom apparatus (venom gland, venom duct, and venom reservoir) are shown in magenta. **C** Proteo-transcriptome data used as a base for our study is illustrated in a modified graphic. Only proteome-verified transcripts of the venom profile described in von Reumont et al. [27] are shown with their expression levels on the x-axis. The three single ICK domain protein families xibalbin₁, xibalbin₂ and xibalbin₁₃ are highlighted. The fourth family of knottin-like proteins, xibalbin₃, which is a double ICK-like domain peptide and not the subject of this study, is indicated in gray

proteomically [27]; see Figs. 1 and 2. Additionally, we used transcriptomes of whole animals, including venom systems, from *Lasionectes entrichoma*, *Morlockia williamsi*, *Godzillignomus frondosus*, and *Pleomothra aplocheles* that have been published [33, 40]. To identify venom proteins in these published data, an automated

search pipeline [41] was employed utilizing hmmer-based identification resulting in final alignments of xibalbins (Fig. 2); see Methods for further details.

Transcripts of xib₁ were found in four of the five remipede transcriptomes, exhibiting higher sequence variation than xib₁₃. Both share an identical scaffold with

(See figure on next page.)

Fig. 2 Alignments of xibalbin variants. **A** Xib₁ and xib₁₃ sequences identified in all remipede transcriptomes and a representative omegatoxin sequence from funnel web spiders (*Agelena*). Signal peptide, propeptide, and mature sequence are indicated on top of the sequences. The proteome-verified xib₁ and xib₁₃ sequences that were synthesized from *X. tulumensis* are highlighted by black boxes and shown in bold. **B** Xib₂ sequences identified in *X. tulumensis*. The sequence that was proteomically verified and synthesized is indicated by a black box. We synthesized two variants that differ in the prediction of the mature sequence as shown. Signal peptide, propeptide, and mature regions in **A** and **B** were separately aligned using mafft-L-INS-I. The asterisk indicates the intermediate xibalbin form that is more similar to ten-cysteine scaffolded sequences while having only eight cysteines

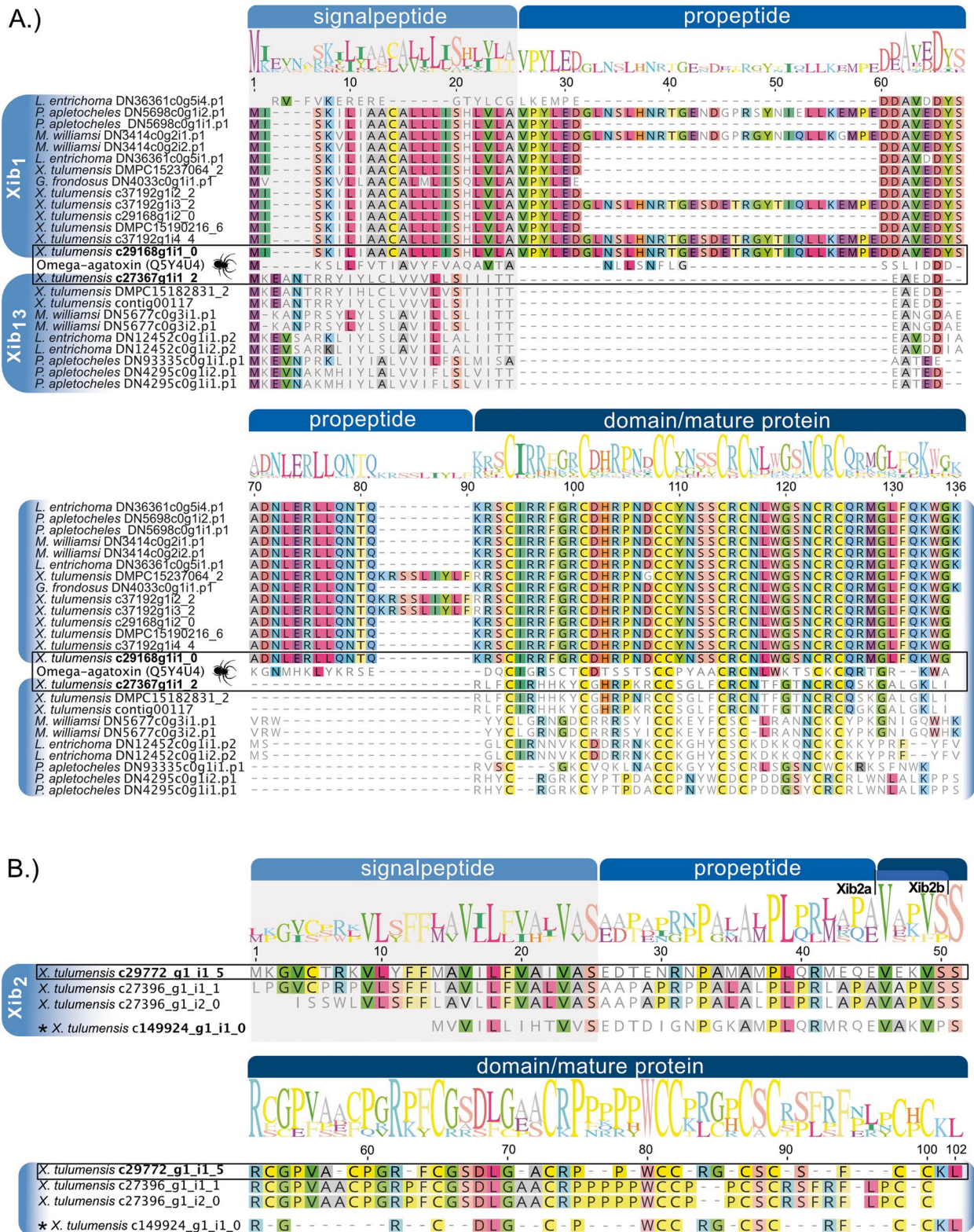


Fig. 2 (See legend on previous page.)

eight cysteines in the mature peptide (see Fig. 2). Similar sequences to xib₂ or xib₃ (which feature a double ICK-like domain) were not recovered in the four other remipedes, except for *X. tulumensis* (see Fig. 2). No other ICK groups with different scaffolds were found, such as the known six-cysteine backbones from insects or cone snails [26, 27].

Prediction and synthesis of xib₁, xib_{2a}, and xib₁₃ mature sequences

The mature sequences for chemical synthesis were predicted using the xibalbin alignments including all transcripts from the five available remipede species; see Fig. 2. Only transcripts with signal peptides described in the proteo-transcriptomic study [27] were considered. The transcripts obtained from the four reassembled novel remipede transcriptomes (besides *X. tulumensis*) guided us additionally to identify mature sequences of representative peptide variants; see Fig. 2 and “Methods.” The xibalbin₂ variants that we name xib_{2a} and xib_{2b} derive from the same sequence but differ in two ambiguously predicted propeptide cleavage sites (Fig. 2). All xibalbin variants were produced synthetically by non-selective refolding; for details, see “Methods.” It has to be noted that the purity of the products differs (Xib₁: 88.0%, xib₁₂: 84.9% purity, xib_{2a}: 99.9%, xib_{2b}: 74.4%) and that the purity < 75% for xib_{2b} is less ideal for bioactivity tests; see Additional File 1: Figure S1.

Xib₁, xib₂, and xib₁₃ strongly inhibit voltage-gated potassium channels and mildly inhibit selected sodium channels while they show no inhibition of calcium channels

We tested the xibalbin variants on a broad selection of voltage-gated potassium (Fig. 3), sodium (Fig. 4), and calcium channels (Fig. 5). The relevant channels were exogenously expressed in *Xenopus laevis* oocytes, and their activities were measured using the two-electrode voltage clamp technique.

Xib₁ and xib₁₃ were found to exhibit a potent inhibition on voltage-gated potassium channels (Kvs) and a mild inhibition on voltage-gated sodium channels (Nav). In contrast, xib_{2a} and xib_{2b} displayed a preference for a limited range of Kvs. Xib_{2a} specifically targeted the Nav1.4 isoform with a high degree of selectivity, while xib_{2b} inhibited solely Kvs. Notably, no detectable activity was observed on T-type calcium channels Cav3.1, Cav3.2, and Cav3.3 (Fig. 6).

Among the Kvs, the highest inhibitory activity of xib₁ (1 μM) was seen on Kv1.6 (74.1 ± 4.1%), followed by Kv1.1 (72.8 ± 3.3%), Kv1.3 (62.0 ± 1.3%), and Kv1.2 (50.2 ± 2.6%). On Navs, Nav1.5 was the most affected isoform (26.1 ± 1.8%), while Nav1.4 (21.8 ± 3.3%),

Nav1.2 (15.8 ± 4.4%), BgNav (8.2 ± 0.6%), and Nav1.6 (5.7 ± 1.2%) were also inhibited. Conversely, Kv1.1 was the most affected Kv isoform by xib₁₃ (85.1 ± 1.7%), followed by Kv1.6 (83.0 ± 2.4%), Kv1.2 (69.3 ± 5.7%), and Kv1.3 (53.5 ± 4.4%). Regarding Nav isoforms, the insect channel BgNav was the most sensitive for this peptide (41.8 ± 4.3%), followed by Nav1.4 (33.0 ± 2.4%), Nav1.5 (28.2 ± 3.4%), Nav1.2 (15.6 ± 2.6%), and Nav1.6 (10.7 ± 0.9%).

Xib_{2a} and xib_{2b} demonstrated a predominant interaction with Kv channel isoforms, specifically Kv1.6, which exhibited the most notable effect (73.2 ± 7.5% and 75.9 ± 4.0%, for xib_{2a} and xib_{2b}, respectively). Xib_{1a} also inhibited Kv1.3 (40.6 ± 6.0%), Kv1.2 (30.0 ± 7.1%), and Kv1.1 (20.0 ± 2.2%). Additionally, xib_{2a} displayed a minor degree of inhibition on Nav1.4 (9.7 ± 1.1%) in addition to the Kv channels. Xib_{2b} exclusively affected Kvs, while also inhibiting Kv1.2 (47.0 ± 1.6%), Kv1.3 (28.5 ± 2.5%), and Kv1.1 (8.7 ± 0.5%).

Furthermore, the peptide's impact on Nav channels was assessed by analyzing the current–voltage relationships of xib₁, xib₁₃, and xib_{2a}, providing insights on its ion channel blocking mechanisms (Fig. 7). The data at V_{half} indicates that the peptides serve primarily as pore blockers for the majority of Nav isoforms since most blocked Nav channels did not present a notable shift in their activation and steady-state inactivation curves, when compared to control (Tables 1 and 2).

However, xib₁ significantly shifted the V_{half} of inactivation of Nav1.2 (−45.9 ± 0.2 mV to −55.5 ± 0.2 mV) and the V_{half} of activation of Nav1.5 (−29.3 ± 0.1 mV to −23.5 ± 0.1 mV). Additionally, Xib₁₃ significantly shifted the V_{half} of inactivation of Nav1.4 (−42.5 ± 0.2 mV to −48.4 ± 0.2 mV) and Nav1.5 (−53.1 ± 0.2 mV to −59.4 ± 0.1 mV), as well as the V_{half} of activation of Nav1.5 (−29.9 ± 0.1 mV to −24.0 ± 0.1 mV) and the insect channel BgNav (−27.6 ± 0.1 mV to −19.9 ± 0.1 mV).

Xib_{2a} solely inhibited the Nav1.4 isoform (Fig. 7 C) and significantly altered its V_{half} of activation (−23.0 ± 0.1 mV to −17.6 ± 0.1 mV), with no notable shift of the V_{half} of inactivation (−44.6 ± 0.2 mV to −44.9 ± 0.3 mV). Notably, these data suggest that besides interacting with the pore region of these Nav isoforms, by reducing the flow of ions through the channel, xibalbins may also interact with the voltage sensor domain of some Nav isoforms (Figs. 6 and 7). Nonetheless, additional studies are needed to fully elucidate their precise mechanism of action.

Xib₁, xib₁₃, and xib₂ do not show overt cytolytic or cytotoxic activity

Having characterized the primary structure of xibalbins and having tested them on selected ion channels, we aimed to determine the biological activity of xibalbins on

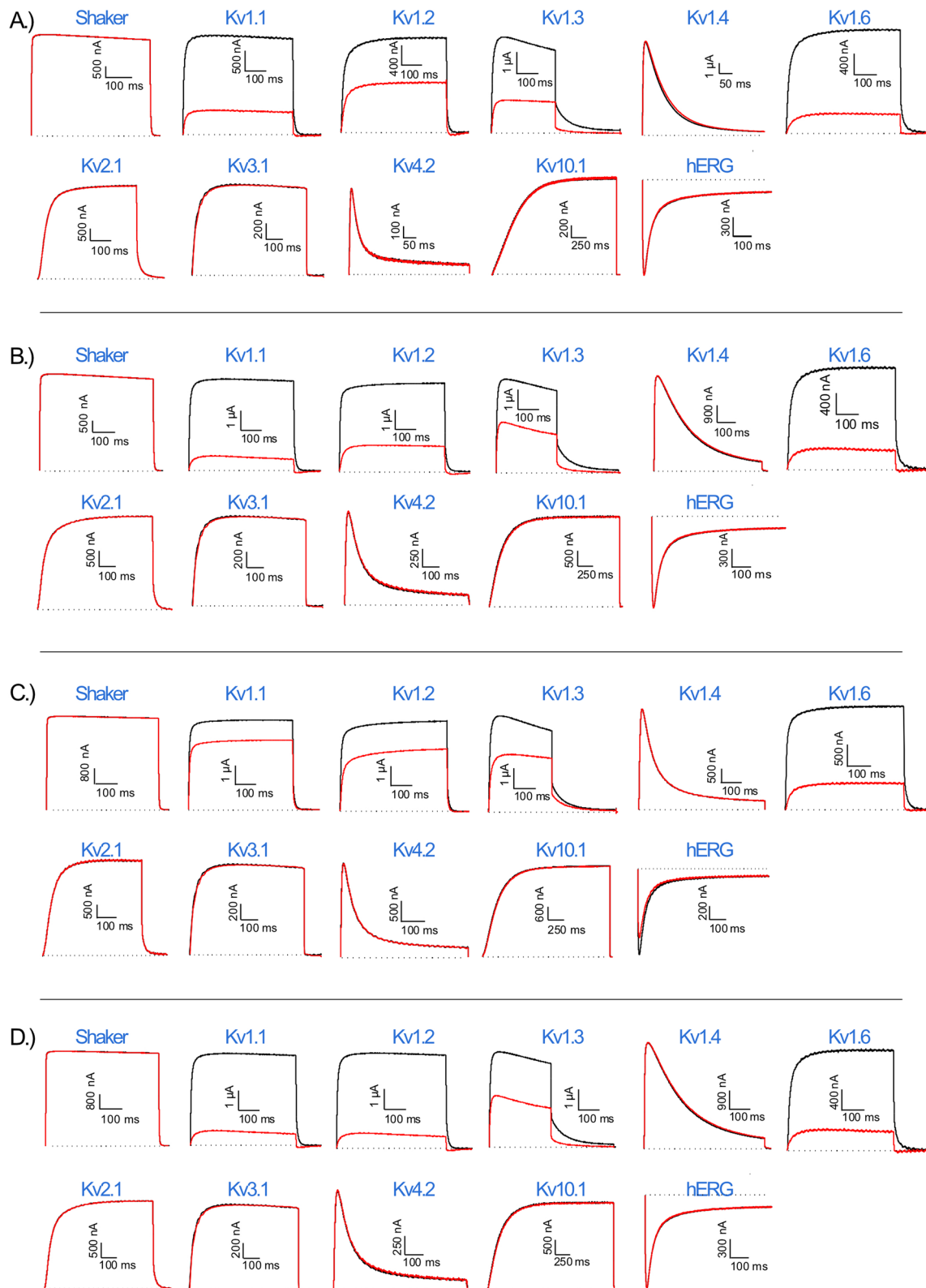


Fig. 3 Electrophysiological characterization of xib₁ (A), xib₁₃ (B), xib_{2a} (C), and xib_{2b} (D), at 1 μM, on a panel of Kv channels. The black lines represent the control condition, while the red lines indicate the current obtained after the addition of each peptide. The dotted lines represent the 0 current level. The graphs illustrate the effects obtained in a series of at least three independent experiments ($n \geq 3$); see “Methods” and Additional File 2: Table S1 for individual data values

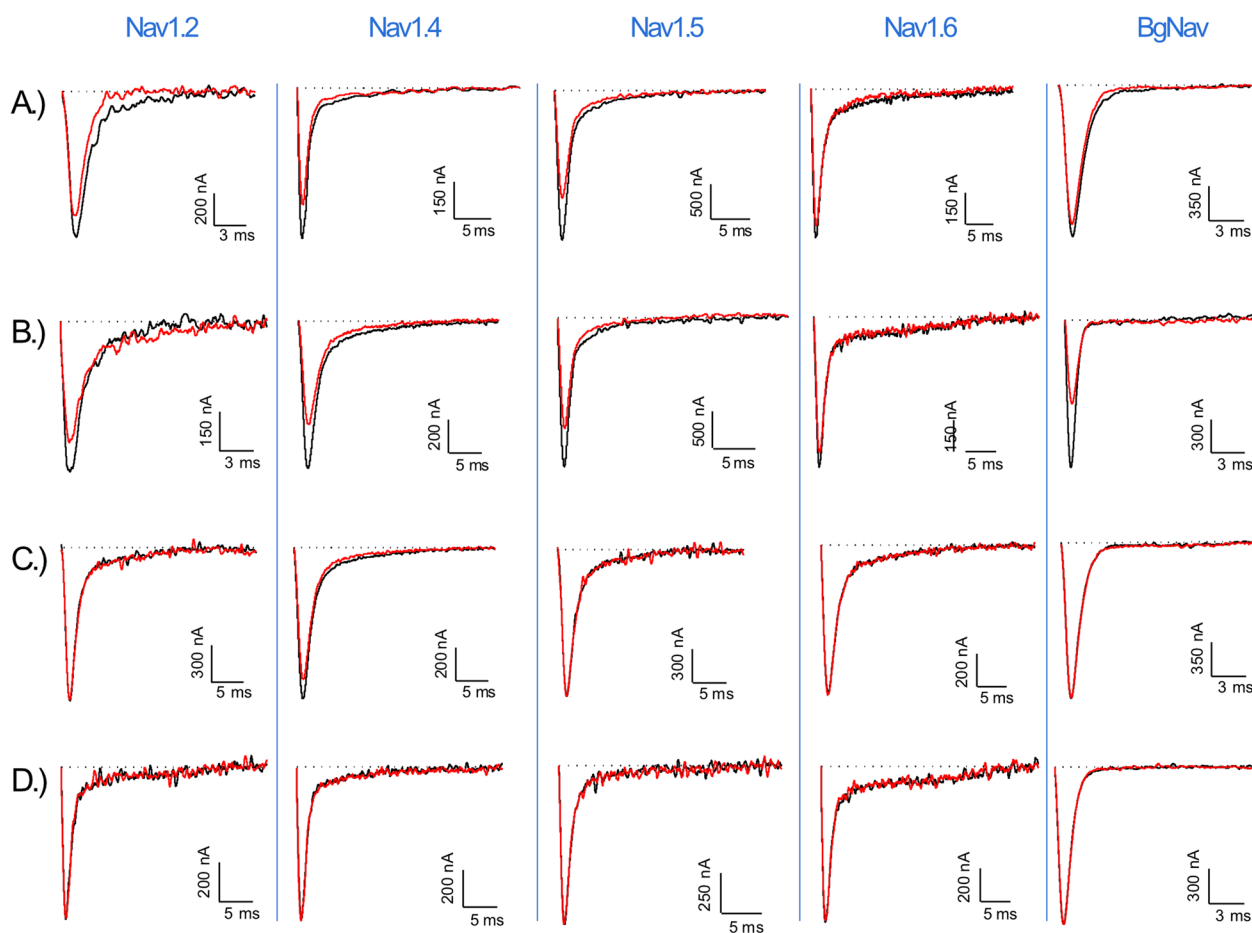


Fig. 4 Electrophysiological characterization of xib_1 (A), xib_{13} (B), xib_{2a} (C), and xib_{2b} (D), at $1 \mu\text{M}$, on a panel of Nav channels. The black lines represent the control condition, while the red lines indicate the current obtained after the addition of each peptide. The dotted lines represent the 0 current level. The graphs illustrate the effects obtained in a series of at least three independent experiments ($n \geq 3$); see “Methods” and Additional File 2: Table S1 for individual data values

the primary cells of adult male rats. The diverse interactions with voltage-gated ion channels suggest that xibalbins have effects not only on electrically active cells such as neurons and cardiomyocytes but also on kidney cells. Consistent with previous studies on other ICK toxins, we evaluated the activity of xibalbins on cultured sensory neurons [42–44].

We initially determined the cytotoxic effects of xibalbins on primary sensory neurons from adult male rats cultured *in vitro* [2]. Sensory neurons exhibit increased sensitivity to changes in size or loss of attachment following exposure to cytotoxic levels of calcium [45]. We exposed overnight cultures of dissociated rat dorsal root ganglions (DRGs) to xibalbins for 5 and 30 min. Subsequently, all cells were fixed and immunocytochemically stained for the neuronal marker UCHL1 to identify neurons. The entire culture was digitally

scanned using high content imaging (HCI) microscopy, and cell numbers, UCHL1 staining per cell, and cell size was analyzed. No loss of neurons was induced by either of the tested xibalbins, even at the highest concentration of $0.8 \mu\text{g}/\mu\text{L}$ (Additional File 3: Figure S2). Additionally, no differences were observed in the size distribution (Additional File 4: Figure S3 A, C) or the staining of the neuronal marker UCHL1 (Additional File 4: Figure S3 B, D). We further investigated the potential toxicity of xibalbins in monocyte/macrophage-like cells (RAW264.7) and human microvascular endothelial cells (HMEC); see Additional File 5: Figure S4. The viability of RAW264.7 cells was detected using a formazan-based assay, while the proliferation of HMECs was assessed by measuring the number of crystal violet-stained cells. The tests did not detect any significant cytotoxic activity of the tested xibalbins.

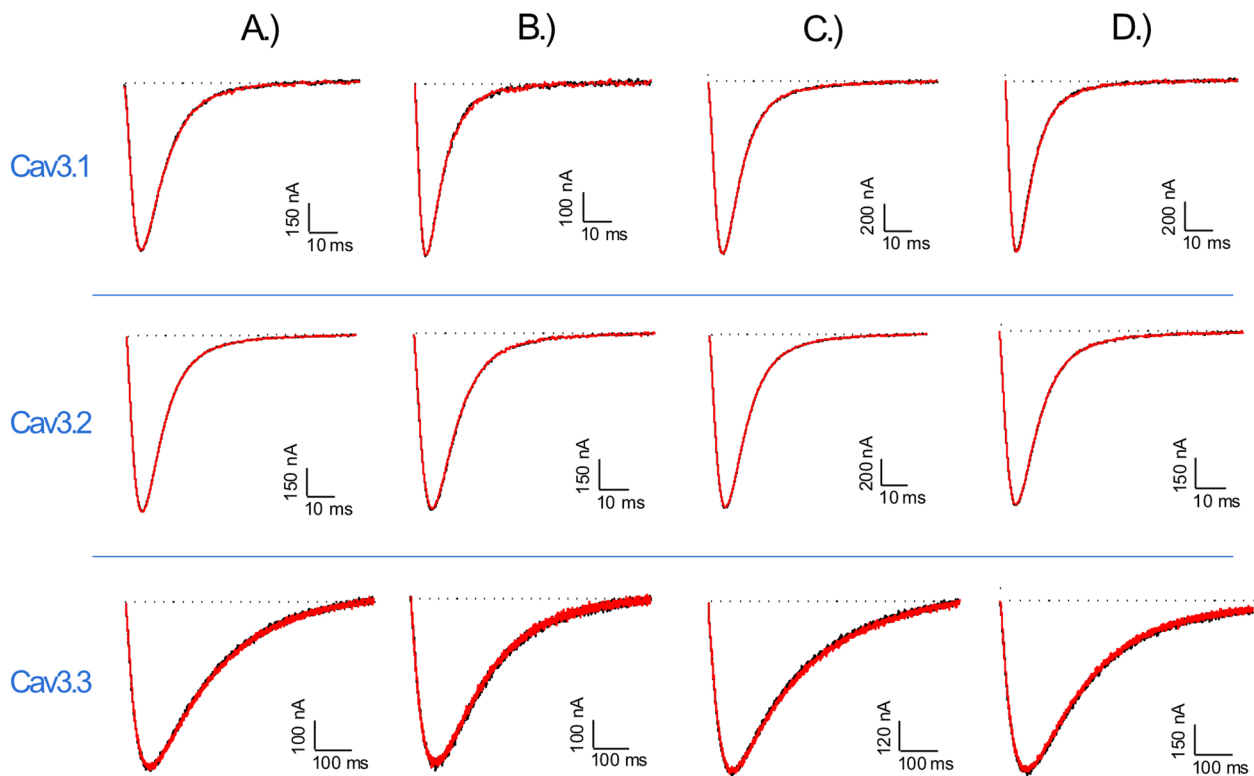


Fig. 5 Electrophysiological characterization of xib₁ (A), xib₁₃ (B), xib_{2a} (C), and xib_{2b} (D), at 1 μ M, on Cav3.1, Cav3.2, and Cav3.3. The black lines represent the control condition, while the red lines indicate the current obtained after the addition of each peptide. The dotted lines represent the 0 current level. The graphs illustrate the effects obtained in a series of at least three independent experiments ($n \geq 3$); see “Methods” for details

Xib₁ and xib₁₃ activate PKA-II and Erk1/2 in sensory neurons, xib₂ does not

Knottins have been demonstrated to modify neuronal activity by acting on voltage-gated ion channels. To gauge sensory neuron activity in response to various activating stimuli, including electrical activity, phosphorylation state detection of protein kinase A type II (PKA-II) and MAP kinase Erk1/2 can act as surrogate measurements [42, 46–48]. Consequently, we tested for increased phosphorylation states in a concentration-dependent manner following exposure to xibalbins. Dissociated DRG neurons were cultured overnight and then exposed to increasing concentrations of the corresponding xibalbins for 5 min and 30 min, respectively. As a positive control, forskolin (Fsk) was also used to induce cAMP synthesis [49, 50]. The activity of PKA-II was monitored by antibodies directed against the phosphorylation site of the inhibitory regulatory subunits RII α / β , which is exclusively accessible when the catalytic kinase domain is released during kinase activation [42]. For measuring Erk1/2 activity, phospho-sites on Erk1/2 (T202/Y204) were monitored through immunofluorescence, as these sites are phosphorylated during activation [51, 52]. Cellular images were captured using HCI microscopy

(Fig. 8A), and the average intensity of each phospho-antibody was quantified (Fig. 8B).

Xib₁₃ induced an increase in phospho-PKA-II intensity in a concentration-dependent manner, following exposure for 5 min at 0.4 μ g/ μ L, up to 1.21-fold ($q=3.29$). Similarly, at a concentration of 0.8 μ g/ μ L (148 and 74 μ M), the intensity increased up to 1.21-fold ($q=4.17$); see Fig. 8C. No change was observed after 30 min of exposure (Fig. 8D). The phosphorylation signal of Erk1/2 (pErk1/2) increased significantly with xib13 after 5 and 30 min, up to 2.5- and 2.3-fold, respectively ($q=4.54$ and 4.32). This effect occurred at a concentration of 0.8 μ g/ μ L (148 μ M); see Fig. 8E, F.

At the highest tested concentration of 0.8 μ g/ μ L (154 μ M), xib₁ caused a significant increase in pErk1/2 intensity by 2.17-fold ($q=4.07$); see Fig. 8F. However, no changes were observed in the intensity of either phospho-PKA-II or pErk1/2 with xib2a and xib2b exposure at either of the two exposure times (Fig. 8C-G).

Xibalbins induce Erk1/2 and PKA-II activation in primary nociceptive and non-nociceptive sensory neurons

Cultures of primary sensory neurons consist of a variety of different neuron subtypes. This includes large-sized

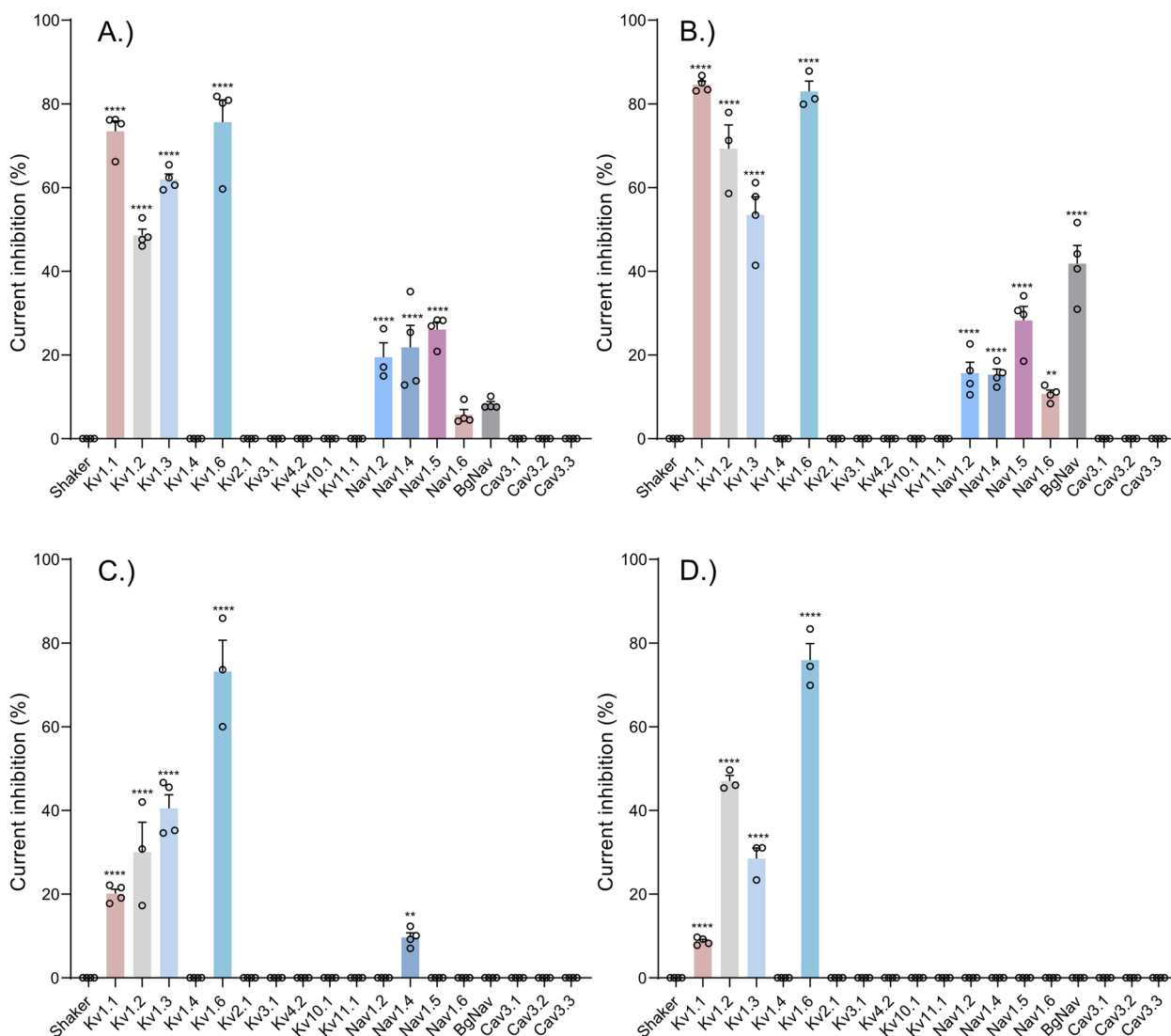


Fig. 6 Effect of xib₁ (A), xib₁₃ (B), xib_{2a} (C), and xib_{2b} (D), at 1 μM versus control, on a panel of voltage-gated potassium (Kv), sodium (Nav), and calcium (Cav) channels. (n ≥ 3) ± S.E.M.; S.E.M standard error of the mean. **p < 0.01; ****p < 0.0001. Differences in ionic currents between control and sample conditions were compared by one-way ANOVA, followed by Dunnett’s multiple comparisons test. Differences were considered statistically significant when p < 0.01. See “Methods” and Additional File 2: Table S1 for individual data values

non-nociceptive and small-sized nociceptive neurons. To characterize if xibalbins activate either one or both neuron subtypes, we analyzed the response according to the cell size. Forskolin used as a positive control to increase phospho-PKA-II activity did not show a prevalence and activated both small and large-sized sensory neurons (Fig. 8G, H). Upon testing with the highest concentrations, xib₁ and xib₁₃ also showed increased phosphorylation signals in both small-sized and large-sized sensory neurons (Fig. 8, H). Therefore, it can be concluded that xib₁ and xib₁₃ act on both nociceptive and non-nociceptive neurons.

No signaling induced by pain-inducing mediators

Xibalbins that modulate sensitization signaling in non-nociceptive and nociceptive sensory neurons suggest the involvement of these toxins in sensation. Therefore, we conducted further tests on pain-related cellular activity including also non-neuronal cells such as HEK293, RAW264.7 macrophage cell line, and leukocytes. Pain-inducing mediators such as bradykinin, prostaglandin E2, LPS, and TNF act by, e.g., increasing Ca²⁺ influx through calcium channels, leading to a significant increase in intracellular calcium ([Ca²⁺]_i), by an increase of cyclic adenosine monophosphate (cAMP) synthesis, and/or by

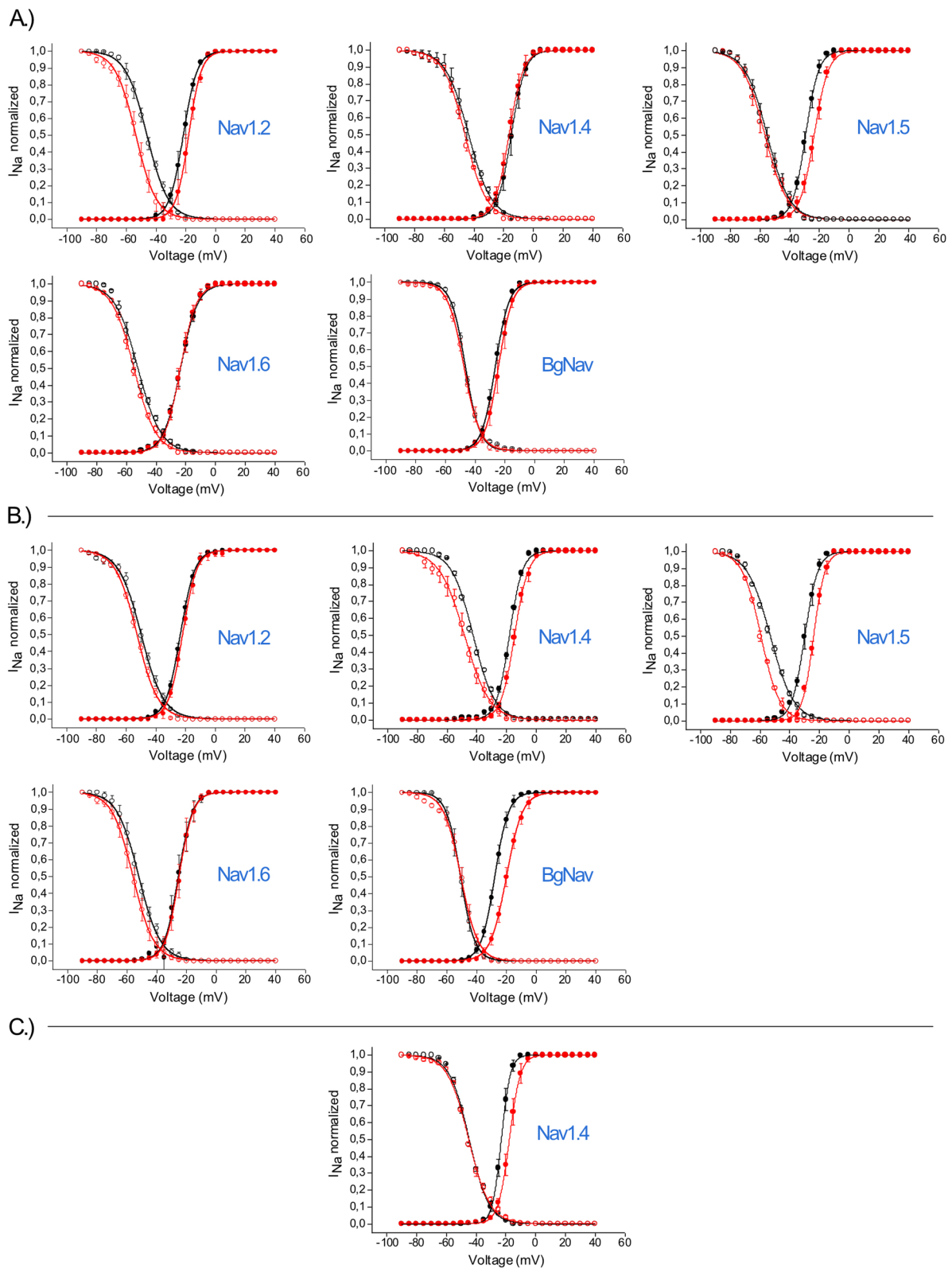


Fig. 7 Activation (closed symbols) and steady-state inactivation (open symbols) curves in control (black) and toxin (red) condition for each Nav channel in the presence of 1 μ M of *xib*₁ (A), *xib*₁₃ (B), and *xib*_{2a} (C). ($n \geq 3$) \pm SEM; SEM standard error of the mean. Statistics were calculated using one-way ANOVA, followed by Tukey's multiple comparisons test. Differences were considered statistically significant when $p < 0.01$; see Tables 1 and 2. See "Methods" and Additional File 2: Table S1 for individual data values

Table 1 Shifts in current–voltage relationships of voltage-gated sodium channels in control (ND96) and in the presence of 1 μM xib₁. ** $p < 0.01$, Fig. 7A

Channel isoform	V_{half} activation (mV \pm SEM)			V_{half} inactivation (mV \pm SEM)		
	Control (ND96)	Xib ₁ (1 μM)	Shift (mV)	Control (ND96)	Xib ₁ (1 μM)	Shift (mV)
Nav1.2	-21.5 \pm 0.1	-19.3 \pm 0.1	3.8	-45.9 \pm 0.2	-55.5 \pm 0.2	-9.6**
Nav1.4	-14.9 \pm 0.1	-16.4 \pm 0.1	-1.5	-43.6 \pm 0.2	-46.0 \pm 0.2	-2.4
Nav1.5	-29.3 \pm 0.1	-23.5 \pm 0.1	5.8 (ns)	-56.6 \pm 0.2	-55.1 \pm 0.2	1.5
Nav1.6	-25.5 \pm 0.1	-23.6 \pm 0.1	1.9	-52.2 \pm 0.3	-54.8 \pm 0.1	-2.6
BgNav	-26.2 \pm 0.1	-24.1 \pm 0.1	2.1	-46.4 \pm 0.1	-47.4 \pm 0.1	-1.0

Table 2 Shifts in the current–voltage relationship of voltage-gated sodium channels in control (ND96) and in the presence of 1 μM xib₁₃. ** $p < 0.01$; *** $p < 0.001$, Fig. 7B

Channel isoform	V_{half} activation (mV \pm SEM)			V_{half} inactivation (mV \pm SEM)		
	Control (ND96)	Xib ₁₃ (1 μM)	Shift (mV)	Control (ND96)	Xib ₁₃ (1 μM)	Shift (mV)
Nav1.2	-23.3 \pm 0.1	-21.8 \pm 0.1	1.5	-49.7 \pm 0.2	-52.5 \pm 0.2	-2.8
Nav1.4	-18.1 \pm 0.1	-14.7 \pm 0.1	3.4	-42.5 \pm 0.2	-48.4 \pm 0.2	-5.9**
Nav1.5	-29.9 \pm 0.1	-24.0 \pm 0.1	5.9***	-53.1 \pm 0.2	-59.4 \pm 0.1	-6.3***
Nav1.6	-25.3 \pm 0.3	-24.8 \pm 0.1	0.5	-52.0 \pm 0.2	-55.9 \pm 0.1	-3.9
BgNav	-27.6 \pm 0.1	-19.9 \pm 0.1	7.7***	-50.6 \pm 0.1	-50.4 \pm 0.2	0.2

induction of NO synthesis [53]. Such elevated levels of intracellular Ca^{2+} , cAMP, or NO can contribute directly and indirectly to an increase in neural activity. Consequently, this can lead to a heightened perception of pain, which is relayed to the central nervous system via direct and indirect pathways.

We examined the potential of xibalbins in a concentration range of 0.25 to 25 $\mu\text{g}/\text{ml}$ regarding their effects on Ca^{2+} influx in HEK293 cells, which express calcium channels. Forskolin, utilized as the positive control, increased $[\text{Ca}^{2+}]_i$ in HEK293 cells [54]. However, exposure to none of the four xibalbin variants by itself did increase $[\text{Ca}^{2+}]_i$ as measured by Fluo-8 calcium imaging assay. Additionally, none of the xibalbin variants modulated forskolin-induced $[\text{Ca}^{2+}]_i$ increase (Additional File 7: Figure S5 A). We also evaluated the effect of xibalbins on cAMP synthesis. However, xibalbins had no effect on increasing cAMP synthesis in HEK293 cells or on preventing the forskolin-induced cAMP synthesis (Additional File 7: Figure S5 B).

Nitric oxide has a complex and diverse role in pain modulation [55]. Our study reveals that xibalbins did not induce NO synthesis in RAW264.7 macrophages and is ineffective in preventing LPS-induced NO synthesis. Additionally, xibalbins showed no cytotoxic effects in RAW264.7 macrophages (Additional File 7: Figure S5 C).

Finally, we analyzed the effects of xibalbins on the leukocyte adhesion to the vascular endothelium, which is a critical step in the inflammatory response of inflamed tissues. Xibalbins were analyzed for their ability to alter the adhesion of human monocytic (THP-1) cells onto a TNF-activated endothelial cell monolayer (Additional File 5: Figure S4). Thus, we do not find xibalbins to have an impact on Ca^{2+} , cAMP, and NO signaling in the cell types analyzed. They do not interfere with the adhesion of leukocytes to endothelial cells. All individual values for these experiments are given in Additional File 8: Table S3.

Diversity and evolutionary origins of ICK-like xibalbins

To explore the diversity and evolutionary origins of all ICK-like xibalbins, we aligned all full protein sequences from the five remipede species (see Fig. 2) with published ICK peptide sequences from arthropods, see “Methods”. These complementary arthropod sequences include confirmed and predicted ICK peptides from venomous and non-venomous crustaceans, insects, myriapods, and chelicerates. The additional sequences were acquired from two studies that collated ICK peptides from pan-crustaceans and arthropods [27, 56] to reconstruct a maximum likelihood-based phylogenetic tree; see

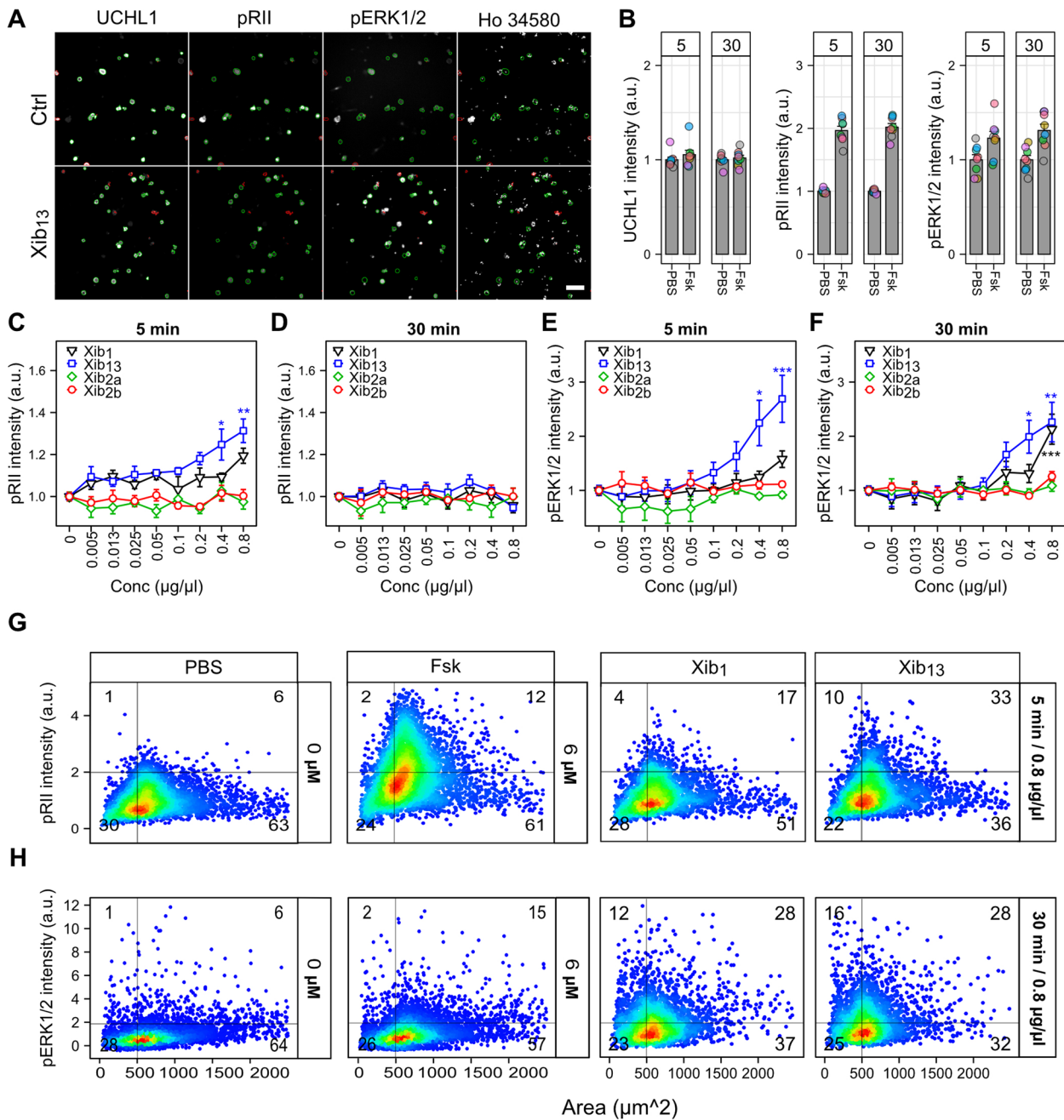


Fig. 8 **A** Representative images of rat DRG neurons stimulated with PBS (Ctrl) and *xib*_{1b} (0.8 µg/µL). Cells were stained for UCHL1, pRII, pERK1/2, and Hoechst followed by fixation and staining with standard immunocytochemistry protocols. Green-encircled neurons indicate automatically selected objects. Scale bar: 100 µm. **B** Mean intensities of UCHL1, pRII, and pERK1/2. The same UCHL1 intensities were observed among tested groups. Forskolin (Fsk), an activator of adenylyl cyclase, was used as a positive control. Fsk at 6 µM concentration induced an increase in pRII and pERK1/2 intensities at 5 and 30 min. Number of analyzed cells per replica: 750 ± 200. Eight independent replicas. **C–F** Concentration responses of xibalbin toxins (0.005 to 0.8 µg/µL) and mean intensities of pRII and pERK1/2 at 5 min and 30 min. **G–H** Size versus pRII and pERK1/2 intensities of cells treated with 0.8 µg/µL of *xib*₁ and *xib*₁₃. Small-sized cells were responding to xibalbins. Statistical significance was assessed using one-way ANOVA with Dunnett’s post hoc test. Data represent mean ± S.E.M (standard error of the mean), *n* = 4, see “Methods” for details and Additional File 6: Table S2 for individual data values

“Methods”. Although our topology remains unresolved in some, especially deeper nodes, we can infer important insights related to the evolution of xibalbins.

Our findings demonstrate that xib_{13} sequences, which are present in all five remipedes, are located in a well-supported clade (88 fast bootstraps) indicating a remipede-specific family that clusters with sequences from the notostracan crustacean *Triops* and basal hexapods that display a similar eight-cysteine scaffold akin to xib_{13} (see Fig. 9). Xib_1 sequences (with their eight-cysteine scaffold similar to xib_{13}) constitute compared to xib_{13} a more distinct, strongly supported clade (97 fast bootstraps); see Fig. 9.

Surprisingly, our phylogenetic analysis demonstrates that xib_2 , the ten-cysteine scaffolded xibalbin limited to *X. tulumensis*, emerges from the eight-cysteine scaffolded xib_1 by an apparent gene duplication. The result is an ancestral, transitional xib_2 sequence (c149924g1i1) with only eight and not ten cysteines which is highly similar in its primary sequence to the other xib_2 family members; see Fig. 9. Finally, we show that xib_3 sequences are closer related to six-cysteine scaffold ICKs from hexapods which indicates a possible six-cysteine variant that occurred in the ancestor of remipedes and hexapods. This result is in line with the findings of Maxwell et al. [56], who propose that xib_3 derives from a domain duplication of an ancestral six-cysteine precursor that has since been lost in *X. tulumensis*. The findings in our phylogenetic analyses, especially the origin of xib_2 from xib_1 , are as well supported in a CLANS analysis using pairwise sequence similarity clustering; see **“Methods”** and Additional File 10: Figure S6.

Machine learning analysis largely corroborates the phylogenetic analysis

To complement our phylogenetic analysis, we employed a novel machine learning (ML) method that constructs a multidimensional space of ICK relationships. This approach utilizes protein language models to generate a 1024-dimensional representation of proteins, known as “protein embeddings” [57]. These embeddings capture similarities based on the model’s understanding of protein structure and function, similar to how natural language processing understands text and

predicts the probability of words appearing in a specific order. This method considers not only the sequence of amino acids but also their positions and interactions, even those separated by longer stretches, and captures nuances in structural and functional properties that are not apparent in direct sequence comparisons. It thus recognizes evolutionary relationships and functional classes of proteins without relying on “traditional” sequence alignment techniques that are based on positional homology; hence, it is termed “sequence independent”. We have to note though that the actual evolutionary process is more complex than what can be shown in visual representations due to the vast number of possible functional ICKs and the constraints of each lineage’s inheritance. For visualization purposes, we condensed this complex space into 3D, with 2D representations used in our figures (Fig. 10).

Our results largely corroborate the phylogenetic findings. Notably, xib_{13} sequences appear as the most ancestral within the remipede-specific cluster, given that xib_{13} represents a subfamily within a larger arthropod ICK subgroup. Furthermore, other remipede ICKs are positioned as close neighbors to xib_{13} , reinforcing this interpretation.

Regarding xib_2 , our analysis revealed an intriguing bifurcation. While one form of xib_2 clusters with other arthropod ICKs, its isolated positioning casts doubt on the significance of these associations. Interestingly, that sequence is the transitional xib_2 sequence with only eight cysteines, which could mean that it exhibits as well a different or intermediate function that is more similar to xib_{13} resulting in this clustering pattern. In contrast, another variant of xib_2 with ten cysteines is near the xib_1 cluster, forming a distinct and tight grouping. This observation provides strong support for the close relationship between xib_1 and xib_2 as suggested by our phylogenetic analysis.

Lastly, the xib_3 sequences displayed a clear clustering pattern by domain. Domain1 sequences of xib_3 were found in close vicinity to a dense cluster of centipede ICKs. This arrangement suggests a potential evolutionary trajectory for xib_3 , likely originating from a centipede ICK and undergoing subsequent domain duplication.

(See figure on next page.)

Fig. 9 Phylogeny of ICK-like proteins in major arthropod groups and knottin-like xibalbins in remipedes. Nodes for which both support values are below 50 are shown in multifurcation, the first number gives the SH-aLRT support in percent, and the second number the fast bootstrap support. The relevant node values for xibalbin protein clades are printed in bold blue. Chelicerates are green, myriapods brown, and crustaceans in blue, while hexapods are colored in black. Major groups are indicated. The cysteine scaffold of ICK-like sequences is shown in white in the dark blue bars. The tree was calculated in IQTREE (-m MFP -alrt 25,000 -B 25000 -bnni -T Auto); for further details, see **“Methods”**. We summarized several nodes for better visualization (triangles); see the full tree file (Additional File 9: Figure S6)

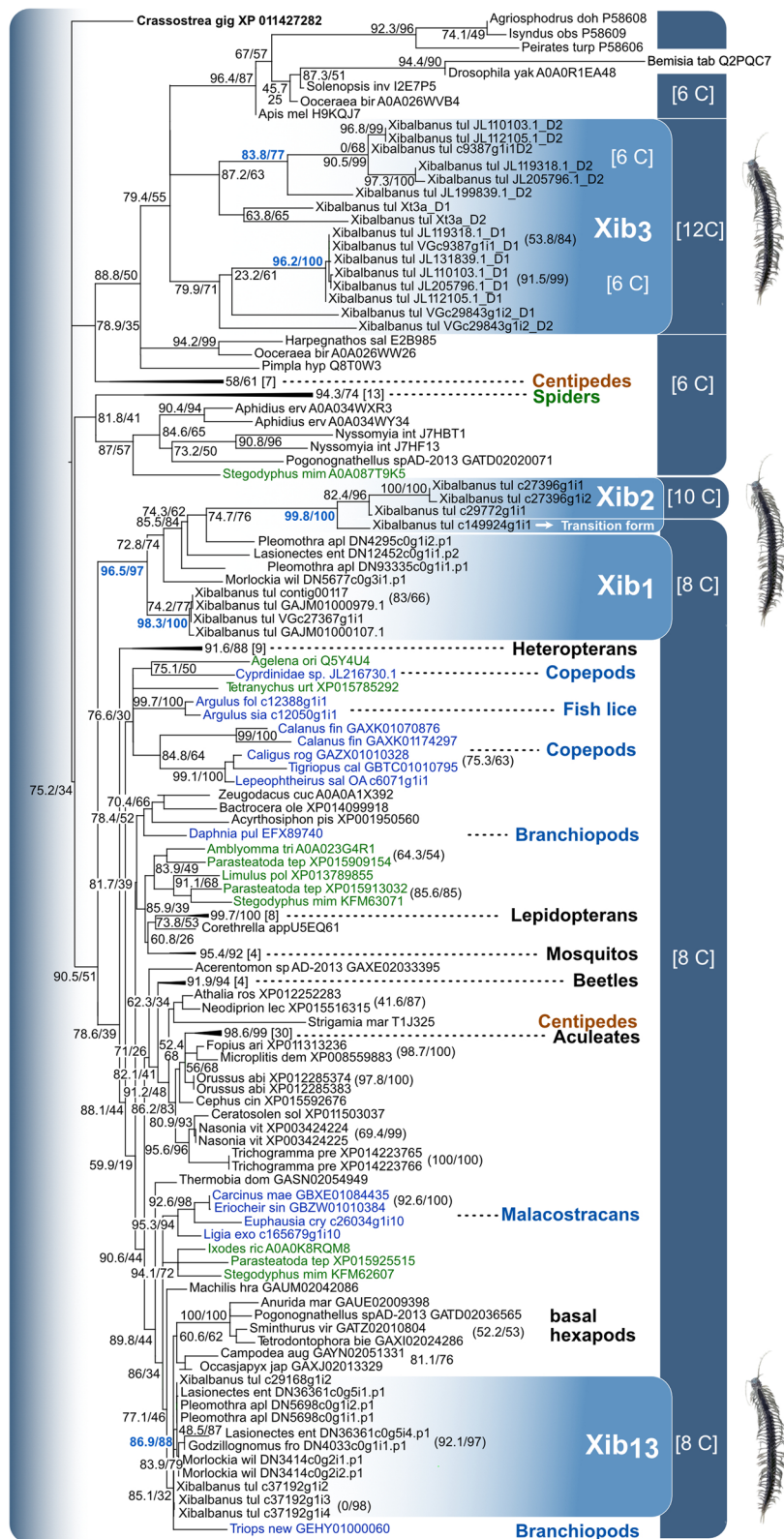


Fig. 9 (See legend on previous page.)

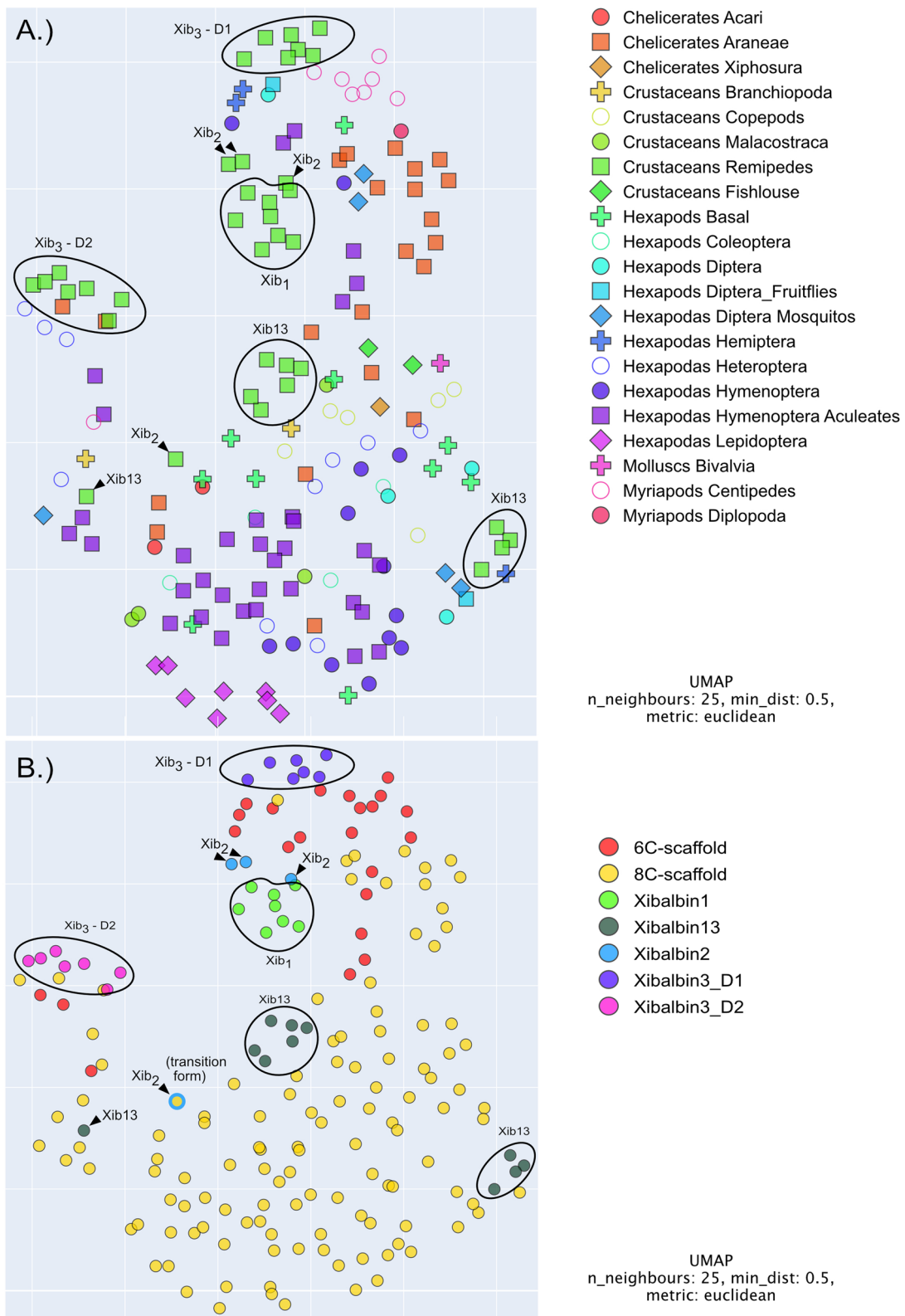


Fig. 10 Machine learning generated protein space representations of xibalbins correspond with gene phylogeny-based grouping. All proteins corresponding with the sequences used to reconstruct the phylogenetic tree are color coded according to their major taxon clade (A) that are also indicated in the phylogenetic tree (Fig. 9) and additionally labeled according to their cysteine scaffold (B). See “Methods” for further details

Discussion

We discuss here predominantly the examined activities of the xibalbin variants in the context of their potential pharmacological application and give first insight on their origins and evolution.

Ion channel activity

Among the tested xibalbin variants, xib₁₃ exhibited the most significant inhibition rates on voltage-gated potassium (Kv) and sodium (Nav) channels (Fig. 6). Intriguingly, despite their broad effects on Kv and Nav channels, none of the xibalbin variants affected T-type voltage-gated calcium channels (Cav3.x); see Fig. 5. Other examples of toxins acting on both sodium and potassium channels come from different species. For example, Nc1a, derived from *Nephila clavata* spider venom, acts on Nav and Kv channels in cockroach dorsal unpaired median neurons [58]. Similarly, HCTx from *Heteractis crispa* sea anemone venom shows remarkable target promiscuity [59, 60].

Both ion channel families (Kv and Nav) were inhibited by xib₁ and xib₁₃ with a preference towards voltage-gated potassium channels and a higher percentage of inhibition when compared to voltage-gated sodium channels. Xib₁ and xib₁₃ inhibit especially Kv1.1 channels which are important in controlling neuronal excitability as they are abundantly expressed in the nervous system [61]. In certain neuroinflammatory diseases such as multiple sclerosis and spinal cord injury, Kv1.1 channels show an altered axonal localization at the juxtaparanodal sites and hereby prevent electrical conduction along the neurons. It is reported that inhibiting Kv1.1 channels results in a reduction of pathological manifestations [62, 63].

In addition, xib_{2a} and xib_{2b} interacted primarily with Kv channels (Kv1.1, Kv1.2, Kv1.3, and Kv1.6) with only Nav1.4 being weakly inhibited by xib_{2a}. The higher and more specific inhibition of Kv1.6 compared to other Kv channels by both Xib₂ variants has direct application potential. Elevated Kv1.6 channel expression is known to be associated with pathological neuronal conduction in epileptic variants of epilepsy. The challenge so far has been that toxins that act on Kv1.6 channels also cross-react with other Kv channel types [64]. The characteristics of xib₂ suggest that this toxin, perhaps with some synthetic modifications, could be of interest for applied studies of Kv1.6. From a biological perspective, xib₂ is among the most highly expressed venom components in *X. tulumensis*, which implies its functional importance linked to the venom biology that remains, however, speculative. Interestingly, similar Kv channels are affected by all xibalbin variants (with the difference that no and only one Nav channel is affected by xib_{2a} and xib_{2b}),

despite their rather different primary sequences. A possible explanation for this phenomenon could be the close phylogenetic relationship between xib₁ and xib₂. We will discuss later that xib₂ originates from xib₁, which could suggest that xib₂ might have been adapted to increase the quantity of Kv-inhibiting toxins in remipede venom.

Interestingly, no xibablin showed inhibitory activity on *Shaker*, an insect Kv channel from *Drosophila melanogaster*; only mammalian voltage-gated potassium channels were affected. On the other hand, besides the activity recorded on mammalian voltage-gated sodium channels, BgNav, an insect Nav from the cockroach *Blattella germanica*, was targeted by Xib₁ and Xib₁₃, being the most affected Nav channel by the latter.

It was recently shown that the double ICK domain-like xib₃ (which was not part of this study) targets RyR channels and promotes calcium release [56]. This suggests that calcium channel targeting is complementarily accomplished by xib₃. Based on this new data, we speculate that the activities on ion channels might be divided among the xibalbins and that they act synergistically: xib₁, xib₁₃ (on Kv and Nav) xib₂ (on Nav), and xib₃ (on RyR). It is important to note though that the folded structures of all of the variants that are tested so far are approximations of the naturally secreted and folded xibalbins, providing first insight into their likely bioactivity. Obtaining crude venom to fractionate the toxins and reveal their natural conformation and bioactivity remains a challenge due to the rarity of remipede individuals in their remote habitats. Although we see no indication of diminished activity, we must note that we could not perform washout or concentration–response experiments to safely exclude artifacts. Nonetheless, the activity of the synthesized variants shows some promising activities for applied research that should be investigated further.

Nociceptive neuron activity by xib₁ and xib₁₃

Sensory neurons exposed to xibalbins did not change in cell number, which indicates the absence of direct cytotoxic effects on cells (Additional File 7: Figure S5). Size and UCHL1 distribution of cells also remained the same among the tested groups suggesting there is no subgroup specific or neural cell death related to our xibalbin variants (Additional File 4: Figure S3). However, this is in line with other studies that test different ICK peptides such as GTx1-15, which has also been shown not to exert cytotoxicity in human cell lines even at high concentrations [65]. The recorded effects on ion channels regulating neuronal membrane potentials makes it interesting to look into the effect of the xibalbin variants on neurons, and we tested their activity on cultured sensory neurons. We observed increased PKA-II and pErk1/2 activity by xib₁ and xib₁₃ but not by xib₂. This is in line with

our data on the ion channel activity because the inhibition of Kv channels by xib₁ and xib₁₃ can prolong the action potential of the neuron, which then leads to activation of PKA-II and Erk1/2. Thouta et al. [66] reported that mice lacking the Kv1.1 coding gene show higher neuronal hyperexcitability, which is in agreement with our data showing that a more potent Kv1.1 inhibitor is a stronger activator of PKA-II and Erk1/2 (Fig. 8C-F and Fig. 8C-D). Whether such an activation is solely driven by the effects on membrane potential-regulating ion channels is not clear. There may also be an additional metabotropic activity of xib₁ and xib₁₃ similar to toxins such as α -latrotoxin or α -Bungarotoxin [66, 67].

We evaluated then the sensitization of rat DRGs by xib₁ and xib₁₃. Analysis of the size of cells reveals that mainly small-sized cells are responding to xibalbin toxins meaning that mostly nociceptive neurons are their predominant target (Fig. 8 G, H). As PKA and ERK activity has been characterized to result in pain behavior [68–71], our results imply that xib₁ and xib₁₃ are able to induce nociceptive neuron activity and are thus potential candidates for pain treatment. It should be noted that the concentrations used were higher than those used in the electrophysiological tests and caution should be exercised in making direct comparisons and biological interpretations. We can only speculate if this activity might reflect predatory or defensive functions of the natural xib₁ and xib₁₃. There is evidence that GPCR and RTK signaling already emerged in unicellular ancestors of metazoan and bilaterian species [72, 73]. In higher organisms, for example in *Aplysia*, GPCR signaling activating the cAMP/PKA pathway has been shown to regulate nociception [74] and the contribution of PKA and ERK to nociceptor hyperexcitability has been demonstrated [75, 76]. These studies suggest that the tested rat DRGs could theoretically reflect also possible activity in prey or predators of *X. tulumensis* [77–79].

Evolutionary perspective on xibalbins

Our phylogenetic analysis illuminates first the possible origins of xib₁₃, which is present in all five remipedes in a well-supported clade. Closely related to xib₁₃ are sequences from early hexapod lineages, indicating that an older xib₁₃ variant existed already in the common ancestor of hexapods and remipedes. More distantly related sequences are from non-venomous crustaceans (malacostracans, notostracans) and chelicerates; however, our topology is not sufficiently resolved in the deeper, more ancestral nodes to draw here further conclusions. Therefore, we can formulate two possible hypotheses on the deeper origin of xib₁₃: either a common ancestral variant already existed in the ancestor of pancrustaceans and chelicerates, or xib₁₃-like proteins evolved convergently

in pancrustaceans and chelicerates. Given the clustering of protein embeddings of xib₁₃ with other arthropodan ICKs in the machine learning analysis of protein space, the former scenario is more likely.

Xib₁ sequences occur in all remipedes except *G. frondosus*. Nevertheless, it appears that xib₁ is a common venom component in remipedes that is more unique to this group, which is reflected in the highly supported clade with remipede-only sequences (Fig. 9) and the protein space clustering (Fig. 10). Given the highly similar eight-cysteine scaffold of xib₁ and xib₁₃, our original hypothesis was that these two peptides are the result of a gene duplication that is followed by subsequent adaptation and high divergence of the sequences within the remipede lineage. However, both phylogenetic and machine learning results reveal separated monophyletic clades for both and thus rather support a separate origin probably from older gene duplication (Figs. 9 and 10). Xib₁ experienced conservatively estimated at least two duplication events as seen in Fig. 9 (two different variants in *Pleomothra*); however, without genome data, this is difficult to interpret.

Surprising is our finding that one duplication event of xib₁ within *Xibalbanus* leads to the origin of xib₂ with an ancestral transitional form (c149924g1i2) that has still eight cysteine patterns similar to xib₁; see Figs. 2, 9, and 10. The primary sequence of this ancestral xib₂ is highly similar to the other xib₂ members but shorter. To draw a certain evolutionary scenario for this finding is somewhat challenging. In general, two novel cysteines could trivially appear by coupled point mutations in the sequence as it was shown in other venom proteins. For example, snake venom phospholipases A2 often evolve novel cysteines for polymerization, while three-finger toxins have evolved a novel inner bond [80, 81]. However, the caveat of this hypothesis is the shorter sequence. A less parsimonious hypothesis is that the duplication of the c149924g1i1 xib₁ gene variant resulted in domain gain that added a sequence stretch in which two further cysteines evolved later. However, without genomic data, any hypothesis remains quite speculative also because the genomic processes that lead to the evolution of ICK peptides and their cysteine scaffolds are not yet studied in detail. Nevertheless, the origin of xib₂ must underlie an important evolutionary constraint. It is a unique component of the venom gland secretion, implying that it is recruited and expressed exclusively in the venom system [27]. However, its high expression (fourth highest expressed venom component in *X. tulumensis*) suggests that it may be functionally more important than xib₁₃ and xib₁. The reasons for this, such as an adaptation to prey or predator, remain to be uncovered.

Less expressed but also *Xibalbanus*-specific is xib₃, which was not tested in this study but by Maxwell et al.

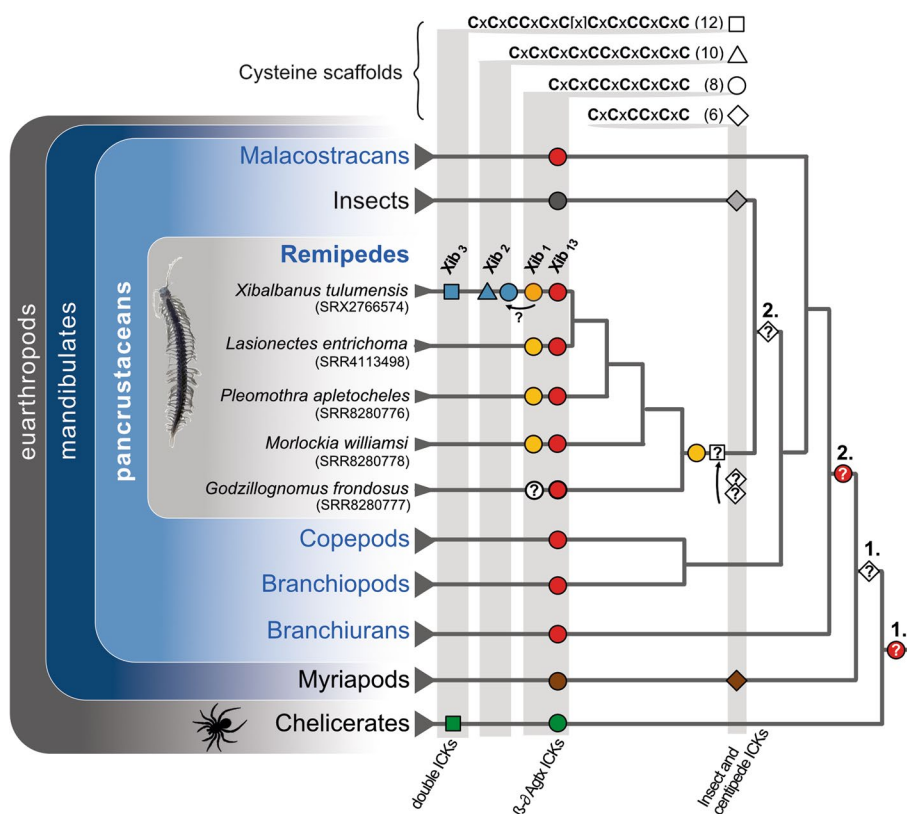


Fig. 11 Synopsis of the evolution of xibalbins. Xib₁ (yellow circle), xib₁₃ (red circle), xib₂ (blue triangle), and xib₃ (blue square) in remipedes are depicted. Sequences with a similar cysteine scaffold (number of cysteins given in brackets) found in insects, other crustaceans, and remaining arthropods are illustrated as well in the same shape but different taxon-specific colors (chelicerates = green, myriapods = brown, insects = gray). Six cysteine scaffolds that are not found in remipedes or crustaceans are shown in the shape of a rhombus. Possible ancestral variants are indicated with a question mark and numbers on top for different alternative hypotheses. The phylogeny is taken from the most recent phylogenomic analysis of pancrustaceans [34]

[56]. We support their findings that the two six-cysteine scaffold domains of this double (domain) knottin are closely related to six-cysteine ICK sequences from insects (Figs. 10 and 11). Maxwell and colleagues argue that they evolved by duplication from an ancestral variant that is lost in *Xibalbanus*. We do not reject this hypothesis, however, given our results, it also implies the loss of six-cysteine variants in all other remipedes and crustaceans. However, our topology is not fully resolved in this part and we refrain from further conclusions.

To better understand the origin and remarkable convergent evolution of ICKs as highly adaptive peptides among major arthropod groups such as insects, crustaceans, and chelicerates, an extended analysis incorporating new proteo-transcriptome venom data from additional remipede species would be advantageous. It is equally crucial to obtain genome data from these arthropods, as recent research has demonstrated that solely utilizing proteo-transcriptome data in addressing gene-specific inquiries including gene origin and duplication

can be flawed [23, 24, 82, 83]. Xibalbins are fundamental ICK-like peptides from an evolutionary viewpoint, providing insights into the emergence and evolution of this diverse toxin category, primarily in remipedes and hexapods, but also among other arthropods (Figs. 9, 10, and 11).

Conclusions

Although structure and function of naturally occurring single domain xibalbin fractions from remipede venom remain to be explored, our results based on synthesized variants support first functional insights that they affect predominantly potassium channels in combination with induced pain. Our results also show how important genome data will be to untangle the origin of xibalbins as part of the ICK-like venom protein family. As remipedes are the sister group to insects, the future identification of their ICK-like venom genes, along with an initial depiction of their conceivable mode of action and their phylogeny, is a crucial stepping stone to better understand the

function and evolution of this hyper-diverse toxin group in remipedes and pancrustaceans.

Methods

Prediction of mature sequences of xibalbin variants and chemical synthesis

From the previous proteo-transcriptomic venom analysis of *X. tulumensis* xib₁ and xib₂ transcripts that are highly expressed and supported on proteome level by MALDI mass spectrometry were used as core sequences for this study [27, 84]. The two xib₁ and xib₁₃ transcripts (c27367_g1_i2_2 and c29168_g1_i2_VG_0) show high sequence similarity with known δ -omegatoxin, which are knottins found in funnel web spiders with an ICK motif based on 8C residues [26, 85]. For xib₂, only one higher expressed transcript (c29772_g1_i1_trinity_VG_ASS_5) was validated on the proteome level. Xib₂ peptides feature an unusual 10C scaffold knottin-like sequence. Currently, no detailed analysis and structural conformation is known for single-domain xibalbins. We predicted the mature sequences of xib₁ and xib₁₃ by aligning these proteins with a representative highly similar structurally known δ -omega toxin peptide from spider venom [85] that was already included in von Reumont et al. (2017) [27, 84] using EMBOSS secondary structure and cleavage site-packages (V1) within the software package Geneious Prime (2022.2.2); see Fig. 2. The domain area of xibalbin₂ was predicted by aligning all transcript variants recovered in the proteo-transcriptomics study [27] and by using the EMBOSS secondary structure and cleavage site packages (V1) within the software package Geneious Prime (2022.2.2). We test here two variations (different cleavage sites) of these sequences with differing lengths of the mature protein; see Fig. 2.

Evaluation of disulfide bonds by mass spectrometry

All chemically synthesized peptides were ordered at Vivitide, Gardner, MA, USA, performing the in-house solid-state synthesis by a standard automated peptide synthesizer. A non-directed refolding process using reduced/oxidized glutathione established thermodynamically stable disulfide bridges. In-house HPLC was run to evaluate the purity for all compounds with the following results: xib₁=88.0%, xib₁₂=84.9%, xib_{2a}=99.9%, and xib_{2b}=74.4% (Additional File 1: Figure S1). To verify sequence and structure, we sequenced all final xibalbin variants by bottom-up mass spectrometry analysis as digested peptides and as intact peptides (top-down). All xibalbin peptide sequences and purity (background noise of non-target fragments) were confirmed by tandem mass spectrometry (MS/MS) of the most abundant peptide fragments (Additional File 11: Figure S8).

The lyophilized undigested peptides were dissolved in ultrapure water (10 mg/mL), and either directly set to final concentration (2 mg/mL) with acidified ammonium bicarbonate buffer (25 mM ABC, 0.1% TFA, pH 7.8) for intact peptide mass analysis, or previously reduced (10 mM dithiothreitol), alkylated (20 mM iodoacetamide), and finally digested (15 ng/ μ L trypsin, Promega, Madison, United States) for bottom-up peptide analysis. In addition, native xibalbin variants were treated by either reduction (10 mM DTT) and alkylation (20 mM IAC) or direct digestion (15 ng/ μ L trypsin, Promega, Madison, USA). The matrix was prepared using a saturated stock solution of α -cyano-4-hydroxycinnamic acid (CHCA) in acetonitrile/ultrapure water (70% acetonitrile with 0.1% trifluoroacetic acid (TFA)). First, samples were spotted by dried droplet onto the ground steel target plate and matrix solution added on top. Mass analyses were performed on a MALDI-ToF/ToF mass spectrometer (ultrafleXtreme, Bruker Daltonics, Bremen, Germany) with the following operating settings: ion source 1=20.00 kV, ion source 2=17.75 kV, lens voltage=8.00 kV, reflector voltage=20.80 kV, optimized pulsed ion extraction time=170 ns, matrix suppression=600 Da, sample rate 5.00 GS/s, analog offset 68.90 mV, and positive reflectron (bottom-up peptide identification) or linear (intact peptide identification) mode. Laser strength and pulse ion extraction time were initially optimized and performance was calibrated using the calibrant peptide standard mixture. Peptides from mass spectra of in-solution digest samples were manually matched against the xibalbin amino acid sequences.

Identification of masses for refolded xib₁ (5163.98 Da), xib₁₃ (5521.05 Da), xib_{2a} (6202.69 Da), and xib_{2b} (5660.60 Da) variants, as well as of xibalbins, whose disulfide bridges were reduced and subsequently alkylated, (xib₁ (5630.35 Da), xib₁₃ (5987.25 Da), xib_{2a} (6784.21 Da), and xib_{2b} (6241.37 Da)) validated the correct number of disulfide bridges by the respective mass difference (Additional File 12: Figure S9). However, we have to note that the exact disulfide connectivity was not determined and that the synthetic peptides may not represent the natural peptides. All mass spectrometry proteomics data (.fid files) have been deposited via the MassIVE partner repository [86] under project name "Non-cytotoxic xibalbin ICK variants from remipede crustaceans" with the data set identifier MSV000091677 [87].

Electrophysiological assays to test for ion channel activity

For the expression of K_v channels rat K_v1.1 (GenBank accession number: NM_173095 [88, 89]), rK_v1.2 (NM_012970 [90, 91]), human K_v1.3 (NM_002232 [92, 93]), rK_v1.4 (NM_012971 [94, 95]), rK_v1.6

(NM_023954 [96, 97]), hK_v2.1 (NM_004975 [98, 99]), hK_v3.1 (NM_004976 [100, 101]), rK_v4.2 (NM_031739 [102, 103]), hKv10.1 (NM_172362 [104, 105]), hERG1 [Kv11.1, (NM_000238 [106, 107])], and *Shaker* IR [from *Drosophila melanogaster*, (NM_167595 [108, 109])], Na_v channels [rNa_v1.2 (NM_012647 [42, 110]), rNa_v1.4 (NM_013178 [111, 112]), hNa_v1.5 (NM_198056 [113, 114]), mNa_v1.6 (NM_001077499 [115, 116]), BgNa_v [from *Blattella germanica*, (DQ466887 [117, 118])] and the auxiliary subunits rβ1 (NM_001271045 [119, 120]), hβ1 (NM_001037 [121, 122]), and TipE [from *D. melanogaster*, (NM_079196 [109, 123])], and Ca_v channels hCa_v3.1 [124, 125], hCa_v3.2 [126, 127], and hCa_v3.3 [128, 129] in *Xenopus* oocytes, the linearized plasmids were transcribed using the T7 or SP6 mMESSEMGEMMACHINE transcription kit (Ambion, Austin, TX, USA). Mature female animals were purchased from Nasco (Fort Atkinson, USA) and were housed in the Aquatic Facility (KU Leuven) in compliance with the regulations of the European Union (EU) concerning the welfare of laboratory animals as declared in Directive 2010/63/EU. The use of *X. laevis* oocytes was approved by the Animal Ethics Committee of the KU Leuven with the license number P186/2019. Stage V–VI oocytes were collected from anesthetized female *X. laevis* frog as previously described [130], with the frogs anesthetized by placement in 0.1% tricaine solution (amino benzoic acid ethyl ester; Merck, USA). Oocyte microinjection was performed using a microinjector (Drummond Scientific®, USA), with a programmed cRNA injection volume of 4–50 nL, depending on the channel subtype. The oocytes were incubated in ND96 solution (96 mM NaCl, 2 mM KCl, 1.8 mM CaCl₂, 2 mM MgCl₂, and 5 mM HEPES, pH 7.4), supplemented with 50 mg/l gentamicin sulfate.

Electrophysiological measurements were performed at room temperature (18–22 °C) using the two-electrode voltage clamp (TEVC) technique. Data were obtained using a GeneClamp 500 amplifier (Axon Instruments, USA), and Clampex9 software (Axon Instruments), responsible for data acquisition and storage. Glass micropipettes were produced using glass capillaries (borosilicate WPI 1B120-6) and drawn in a WPI (World Precision Instruments, USA) manual stretcher. The bath and perfusion solutions were either the previously described ND96 (Na_v and K_v channels) or calcium-free ND96 supplemented with 10 mM BaCl₂ (Cav channels).

Whole-cell currents of oocytes were recorded 1 to 3 days after injection. Current and voltage electrodes were filled with 3 M KCl and their resistance was adjusted from 0.7 to 2.0 MΩ. Currents were sampled at 20 kHz (Na_v channels) and 10 kHz (K_v and Ca_v channels) and filtered using a four-pole Bessel low-pass Bessel filter, at 1 kHz for sodium, and 500 MHz for potassium and

calcium, except for the hERG ion channel, in which the currents were filtered at 1 kHz. Leak subtraction was performed using a -P/4 protocol. K_v1.x currents were evoked by 500 ms depolarizations to 0 mV followed by a 500-ms pulse to -50 mV, from a holding potential of -90 mV. K_v2.1, K_v3.1, and K_v4.2 currents were elicited by 500 ms pulses to +20 mV from a holding potential of -90 mV. Current traces of Kv10.1 were elicited by 2 s depolarization to 0 mV, from a holding potential of -90 mV. Current traces of hERG1 channel were elicited by applying a +40 mV prepulse for 2 s followed by a step of -120 mV for 2 s. Sodium current traces were evoked by a 100 ms depolarization to 0 mV, from a holding potential of -90 mV. The current–voltage (IV) relationships were determined by 100-ms step depolarizations between -90 and +40 mV, using 5 mV increments. For Ca_v channels, current traces were elicited by 700 ms depolarizations to -20 mV from a holding potential of -90 mV. Current values were expressed as means ± SEM of at least three independent experiments. Differences in ionic currents between control and sample conditions were compared by one-way ANOVA, followed by Dunnett multiple comparisons test. The shifts in V_{half} of activation and inactivation of Nav channels were compared by one-way ANOVA, followed by Tukey's multiple comparisons test. Differences were considered statistically significant when $p < 0.01$.

High-content imaging assay for sensory neuron activity

Male Sprague Dawley rats (250–400 g, 8–16 weeks old) were obtained from Envigo. Rats were kept in 12 h of light/darkness cycles. All experiments were performed in accordance with the German animal welfare law with permission of the District Government for Nature and Environment, NRW (84–02.05.20.13.045, 4.18.003). Rats were scarified by slow inhalation of CO₂ which was followed by decapitation. DRGs were extracted from rats, deheated, pooled, and incubated in Neurobasal A/B27 medium (Invitrogen, #12349–015) supplemented with B-27 (Invitrogen #17504), L-glutamine 1:400, L-glutamate 1:270.3, and penicillin/streptomycin 1:100 containing 0.2 U/mL collagenase P (collagenase P, Roche, #1213857) and incubated for 1 h at 37 °C, 5% CO₂. DRGs were dissociated with pasteur pipettes and axon stumps were separated by BSA (Sigma-Aldrich, # A2153-100G) gradient centrifugation (14% BSA, 120 g, 8 min). Cells were resuspended in NBA medium, plated in 96-well imaging plate (Greiner BioOne Sensoplate, Black, #655896) precoated with poly-L-ornithine hydrochloride (0.1 mg/ml Sigma, #P2533)/laminin (5 µg/ml Invitrogen, #23017–015), and incubated overnight at 37 °C, 5% CO₂.

DRGs were stimulated after overnight incubation. Compounds were prepared as tenfold concentrated stock

solutions, diluted in PBS (PAA, cat# H15-002), in v-bottom plates; 50 μ L media from culture wells were mixed with the 12.5 μ L stock solutions, and 50 μ L added back to the respective wells. Stimulation was performed with automated multichannel pipette and cells were kept in heated block during the stimulation. Cells were then fixed for 10 min at RT with paraformaldehyde (final concentration: 4%, Cat# 1.04005) at desired time points. Fixed cells were washed twice with PBS. Following blocking and permeabilization (2% normal goat serum (Dianova, Hamburg, Germany, #005-000-121), 1% BSA, 0.1% Triton X-100 (Roth, Karlsruhe, Germany, #3051.2), 0.05% Tween 20 (Sigma-Aldrich, #P9416)) for 1 h at RT, respective primary antibodies diluted in 1%BSA in PBS was added to the cells and incubated for and overnight at 4 °C. After that, cells were washed three times with PBS (10 min) and secondary antibodies (1:1000, fluorescently labeled) and DAPI (50 ng/ml-1) for 1 h at RT in dark. Finally, cells were washed three times with PBS (10 min) and wells were filled with PBS, sealed, and kept at 4 °C until scanning.

Stained cells were scanned with a CX7-LZR (Thermo Fisher Scientific) HCI system. Images were acquired with a 10 \times objective and analyzed using the cellomics software package (Thermo Fisher Scientific). UCHL1 channel was used as a marker to identify neurons. Object selection was further based on the following criteria: 120–6000 μ m²; circularity: 1–2; length-to-width ratio: 1–2; average intensity: 250–2000; and total intensity: 6 \times 10⁴ to 5 \times 10⁶. The resulting objects were quantified for average object intensity in all other color channels. Untreated wells were used for normalization and compensation was performed for minimizing spill over between channels. All analyses were conducted using R programming language and RStudio as integrated development environment (IDE). One-way ANOVA, Dunnett's test post hoc was performed to evaluate statistical significance between groups. The difference between the two means (D) divided by the standard error of that difference (computed from all the data): $q = D/SED$.

Identification of xibalbin1 and xibalbin2 variants and phylogenetic reconstruction

We then mined identified xibalbin sequences in whole-body transcriptomes of four other published remipede species [33, 40] to identify possible xib_1 , xib_{13} , xib_2 , and finally xib_3 sequence variants via an automated hmmer-search. In brief, available comprehensive alignments of all xibalbin sequences reconstructed from published *X. tulumensis* transcriptome data (SRX2766574) [27, 84, 131] were used to train hmm-models using the av-hmmer-pipeline [41]. The matching sequences were identified in the translated ORFs. Beforehand, the raw read data

of the four remipede species were downloaded from the SRA archive (NCBI): *L. entrichoma* (SRR4113498) [40, 132], *M. williamsi* (SRR8280778) [33, 133], *G. frondosus* (SRR8280777) [33, 134], and *P. apletocheles* (SRR8280776) [33, 135]. The raw reads were quality checked with FastQC [136] and processed with Trimmomatic v0.38 [137] using standard settings except for a chosen quality threshold of phred 30 and a minimum length of 50 bp. The trimmed reads were assembled with Trinity v2.8.4 [138] using standard settings except for a minimum length of 100 bp (Additional File 13: Data S2, Additional File 14: Data S3, Additional File 15: Data S4, Additional File 16: Data S5). Open reading frames (ORF) with a minimum of 40 aa were predicted with Transdecoder v5.0.4 (Additional File 17: Data S6, Additional File 18: Data S7, Additional File 19: Data S8, Additional File 20: Data S9).

All sequences of xib_1 , xib_2 , and xib_{13} alignments (Additional File 21: Data S10, Additional File 22: Data S11, Additional File 23: Data S12) were combined with known ICK toxins and highly similar sequences from non-venomous arthropods available in UniProt combining the sequences used in Maxwell et al. [56, 139] (with separated first and second double ICK domains of xib_3) and von Reumont et al. [27]; see Additional File 24: Data S13. Signal peptide, propeptide, and mature regions were separately aligned for all sequences with optimization strategy for one domain using Mafft-L-INS-I [140] and then concatenated. The phylogenetic tree was reconstructed with IQ-TREE2 [141, 142] on 56 cores using settings for rapid bootstraps with integrated model fitting and branch length optimization (MFP, -B 25000, -bnni, -T 56). The original tree (Additional File 9: Data S1) was condensed for Fig. 9 by collapsing all nodes below a support value of 50. The complementary CLANS analysis was performed with standard settings using the Java version 29.05.2012 and 81,987 rounds [143].

Construction of ICK embedding protein language model space

We leveraged modern advances in machine learning, in particular—in natural language models adopted to work with proteins—protein language models (or pLMs) [144]. These models have been successfully used to create protein space for various datasets, including our own work [23, 81]. It was shown that distance in embedding space correlates with protein function and can be used as an orthogonal signal for clustering proteins into functional families [145].

Here, we used the pLM ProtT5-XL-UniRef50 [144] (in the following ProtT5) to create fixed-length vector representations for each protein sequence (per-protein embeddings) irrespective of its length. To achieve

that, we first created individual vector representations for each residue in a protein and then averaged over all residue embeddings in a protein to derive fixed-length vector representations for single proteins (per-protein embedding) irrespective of a protein's length. As ProtT5 was only trained on unlabeled protein sequences and no supervised training or fine-tuning was performed, there is no risk of information leakage or overfitting to a certain class or label. As a result, every protein was represented as 1024-dimensional per-protein embeddings. Those high-dimensional representations were projected to 3D using UMAP ($n_neighbors=25$, $min_dist=0.5$, $random_state=42$, $n_components=3$) and colored according to their respective group to allow for visual analysis. Embeddings were created using the `bio_embeddings` package [145]. Interactive 3D plots of protein spaces are given in Additional File 25: Data S14 (proteins labeled according to taxa clades and protein families) and Additional File 26: Data S15 (proteins labeled according to cysteine scaffold) and were reconstructed using the algorithm deposited on github: <https://github.com/Rostlab/RostSpace>.

Abbreviations

ICK	Inhibitor cysteine knot
PKA	Protein kinase A
ERK	Extracellular signal-regulated kinase
FSK	Forskolin
LDLa	Low-density lipoprotein receptor domain class A
HCI	High content imaging
UHCL(1)	Ubiquitin C-terminal hydrolase L(1)
DRG	Dorsal root ganglion
HMEC	Human mammary epithelial cells
ORF	Open reading frame
pRII	Phosphorylated regulatory subunit type
TEVC	Two-electrode voltage clamp
KCl	Potassium chloride

Supplementary Information

The online version contains supplementary material available at <https://doi.org/10.1186/s12915-024-01955-5>.

Additional file 1: Figure S1. HPLC spectrograms of all xibalbins. All information and retention times are given in the tables to the right of each spectrogram.

Additional file 2: Table S1. Individual data values of all electrophysiological experiments.

Additional file 3: Figure S2. Number of analyzed cells A) at 5 and B) at 30 min. At different concentrations. There is no significant change in number of cells against control (concentration 0). Statistics: One Way ANOVA, Dunnett's post hoc. Data represent mean \pm s.e.m.

Additional file 4: Figure S3. A) Size and B) UCHL1 intensities of the tested cells among replicas, see Material and Methods. There is no difference on the size and UCHL1 intensities of the tested cells between 4 replicas. C) Size and D) UCHL1 intensities of the tested cells among different time points. Overall, there is no difference in the size and UCHL1 intensities of the tested cells among replicas and tested conditions.

Additional file 5: Figure S4. Effects of xibalbins on cytotoxicity in RAW264.7 macrophages and adhesion of leukocytes onto the vascular endothelium. (i) For the viability assay, RAW264.7 cells were treated with 25 μ g/ml

concentrations of xibalbins for 24 h. Cells were incubated with WST-8 and the formed formazan was detected by absorbance measurements. (ii) For the proliferation assay, HMEC-1 cells were grown in low density and treated after 24 h with the indicated peptide for 72 h. Cells were stained with crystal violet solution. The amount of DNA-bound crystal violet was detected by absorbance measurements. (iii) Xibalbins do not interfere with the adhesion of leukocytes on endothelial cells. THP-1 cell adhesion under static conditions. HMECs were grown to confluence, preincubated with xibalbins for 30 min, and activated with TNF (10 ng/ml) for 24 h. For the leukocyte adhesion assay, untreated THP-1 cells (3×10^4 cells/well) were stained with CellTracker Green (Thermo Fisher Scientific, Frankfurt am Main, Germany) and were allowed to adhere to the treated HMECs for 5 min. The adhesion of leukocytes onto endothelial cells was quantified by fluorescence measurements using a Tecan Infinite F200 Pro microplate reader (Tecan, Männedorf, Switzerland) (excitation: 485 nm, emission: 535 nm). See Additional File 6 for all individual values.

Additional file 6: Table S2. Individual data values of all UCHL1, pRII, pERK1/2 HCIS experiments.

Additional file 7: Figure S5. A) For the induction assay (left panel) HEK293T cells were treated with 4 μ M Fluo-8-AM in 100 μ l HBSS for 1 h, 37 °C. Five images/sec were taken using an ImageXpress Micro Confocal High Content Imaging System. Xibalbins (0.25, 2.5, 25 μ g/ml), DMSO (negative control), or 5 μ M ionomycin (positive control) were added with images taken every second for 20 s. For the inhibition assay (right panel), the peptide-treated samples (30 min) were treated with 5 μ M ionomycin with images taken every second for 20 s. MetaXpress Software Version 6 was used for data analysis. A threshold of fluorescence intensity was defined using cells before treatment, all cells above the threshold level were counted. The number of cells above the threshold in the toxin-treated samples was related to the cells in the DMSO- or ionomycin-treated sample. B) HEK293T cells were transfected with pGloSensor-22F cAMP plasmid (E2301, Promega, Walldorf, Germany) using turbofect reagent (ThermoFisher Scientific, Frankfurt am Main, Germany). cAMP transfected HEK293T cells were incubated in DMEM without phenol red supplemented with pGlo sensor cAMP reagent (E1290, Promega, Walldorf, Germany). Induction and inhibition assay were performed in two steps with the same plate. For the induction assay (left panel), the luminescence was detected (background, 3 measurements every 5 min) and then the xibalbins (0.25, 2.5, 25 μ g/ml) or 5 μ M forskolin were added to detect the luminescence (3 measurements/5 min) using a plate reader (Spark, Tecan, Männedorf, Switzerland). For the inhibition assay (right panel), the xibalbin-treated cells were incubated with 5 μ M forskolin to detect the luminescence (3 measurements/5 min). Luminescence values of xibalbin-treated samples were related to the DMSO- or forskolin-treated sample. C) For the induction assay (left panel), we treated the RAW264.7 macrophages with the xibalbins, DMSO and 100 ng/ml lipopolysaccharide (LPS) (positive control). For the inhibition assay (right panel) cells were 30 min pre-incubated with peptides or control (DMSO) before adding 100 ng/ml LPS. After 24 h NO was determined in supernatants with the Griess method. The NO levels of the xibalbin-treated samples were related to the DMSO- or LPS-treated sample. See Additional File 6 for all individual values.

Additional file 8: Table S3. Individual data values of all RAW246.7 and cytotoxicity experiments.

Additional file 9: Data S1. Phylogenetic tree file of all ICK peptides from remipedes and higher arthropods reconstructed in IQTREE.

Additional file 10: Figure S7. Results of the pairwise sequence similarity clustering analysis using standard setting in CLANS are shown.

Additional file 11: Figure S8. Peptide sequencing of xibalbin variants by MALDI-ToF/ToF mass spectrometry.

Additional file 12: Figure S9. Disulfide bond matching of xibalbin variants by MALDI-ToF/ToF MS.

Additional file 13: Data S2. New de novo assembly of the remipede transcriptome SRR4113498 generated with Trinity, as fasta file. (39.2 MB).

Additional file 14: Data S3. New de novo assembly of the remipede transcriptome SRR8280778 generated with Trinity, as fasta file

Additional file 15: Data S4. New de novo assembly of the remipede transcriptome SRR8280776 generated with Trinity, as fasta file.

Additional file 16: Data S5. New de novo assembly of the remipede transcriptome SRR8280777 generated with Trinity, as fasta file.

Additional file 17: Data S6. Open reading frames predicted with Transdecoder for the new remipede transcriptome assembly SRR4113498, as fasta file. (26.9 MB).

Additional file 18: Data S7. Open reading frames predicted with Transdecoder for the new remipede transcriptome assembly SRR8280778, as fasta file.

Additional file 19: Data S8. Open reading frames predicted with Transdecoder for the new remipede transcriptome assembly SRR8280776, as fasta file.c

Additional file 20: Data S9. Open reading frames predicted with Transdecoder for the new remipede transcriptome assembly SRR8280777, as fasta file.

Additional file 21: Data S10. All xibalbin₁ sequences aligned with Mafft, as fasta file.

Additional file 22: Data S11. All xibalbin₂ sequences aligned with Mafft, as fasta file.

Additional file 23: Data S12. All xibalbin₃ sequences aligned with Mafft, as fasta file.

Additional file 24: Data S13. All xibalbin sequences including xibalbin₃ and other arthropod ICK aligned with mafft, as fasta file.

Additional file 25: Data S14. All sequences in 3D space illustrating functional relations labeled according to taxon and protein family, html file.

Additional file 26: Data S15. All sequences in 3D space illustrating functional relations labeled according to cysteine-scaffold, html file.

Acknowledgements

BMvR likes to thank for work and discussions on the expression of xib₂ variants following members of the Animal Venomics group that he coordinated until the end of 2021 at the Institute for Insect Biotechnology at the JLU Giessen: Anne Paas, Lea Talmann, Kim Kirchhoff, Frank Förster, Tim Lüddecke, and Andre Billion. BMvR and BFH thank Maria Vittoria Modica for her enthusiastic work and efforts in steering the EU COST Action EUVEN (CA19144).

Authors' contributions

Conceptualization, administration, and design of the study by BMvR with input from EA, ELP-J, TH, B-FH, JT, SP, and IK. Methodology and formal analysis by ELP-J, SP, EA, BMvR, B-FH, SS, PE, RF, TH, JJ, IK, and TS. Writing of first draft by BMvR, ELP-J, and EA. TH, B-FH, SS, SP, TS, RF, PE, and AV contributed to the final manuscript. All authors read and approved the final manuscript.

Funding

Open Access funding enabled and organized by Projekt DEAL. AV and BMvR acknowledge generous funding by the Hessen State Ministry of Higher Education, Research and the Arts (HMWK) obtained by Andreas Vilcinskas for the group Animal Venomics within the LOEWE Center "Translational Biodiversity Genomics" at Senckenberg. BMvR acknowledges the toxin synthesis grant he received from LOEWE TBG. ELP-J was supported by São Paulo Research Foundation (FAPESP, scholarship n. 2016/04761–4) and by Coordination for the Improvement of Higher Education Personnel (CAPES, scholarship n. 88881.186830/2018–01). JT was funded by grants GOC2319 N, GOA4919 N, and GÖE7120N (F.W.O.-Vlaanderen). SP is supported by KU Leuven funding (PDM/19/164). This publication is based upon work from COST Action CA19144 EUVEN (European Venom Network), supported by COST (European Cooperation in Science and Technology).

Availability of data and materials

All data generated or analyzed during this study are included in the supplementary information files of this article, including the individual data values of all experiments (Additional File 2: Table S1, Additional File 6: Table S2, Additional File 8: Table S3). The transcriptome assemblies and protein predictions that were generated from published data (see references) are additionally provided in the open-access database ZENODO, <https://doi.org/10.5281/zenodo.7808089> [146]. The proteome data to test the synthesized products is deposited in the MassIVE data repository MSV000091677 (<https://massive.ucsd.edu/ProteoSAFe/dataset.jsp?task=058eae6afbb5402a987e9ca55312f8cc>) [87].

Declarations

Ethics approval and consent to participate

Not applicable.

Consent for publication

Not applicable.

Competing interests

The authors declare they have no competing interests.

Author details

¹Toxicology and Pharmacology - Campus Gasthuisberg, University of Leuven (KU Leuven), Herestraat 49, PO Box 922, 3000 Louvain, Belgium. ²Department of Anesthesiology and Intensive Care Medicine, University Cologne, Translational Pain Research, University Hospital of Cologne, Cologne, Germany. ³Fraunhofer Institute for Translational Medicine and Pharmacology ITMP, Theodor-Stern-Kai 7, 60596 Frankfurt Am Main, Germany. ⁴Institute of Pharmaceutical Biology, Goethe University Frankfurt, Max-Von-Laue-Str. 9, 60438 Frankfurt, Germany. ⁵LOEWE Center for Translational Biodiversity Genomics (LOEWE-TBG), Senckenberganlage 25, 60325 Frankfurt, Germany. ⁶Department of Bioresources, Fraunhofer Institute for Molecular Biology and Applied Ecology (IME-BR), Ohlebergsweg 14, 35394 Giessen, Germany. ⁷Department of Informatics, Bioinformatics and Computational Biology, i12, Technical University of Munich, Boltzmannstr. 3, 85748 Garching, Munich, Germany. ⁸Freie Universität Berlin, Veterinary Centre for Resistance Research (TZR), Robert-Von-Ostertag Str. 8, 14163 Berlin, Germany. ⁹Faculty of Biological Sciences, Institute of Cell Biology and Neuroscience, Goethe, Frankfurt, Max-Von-Laue-Str 13, 60438 Frankfurt, Germany.

Received: 17 February 2024 Accepted: 9 July 2024

Published online: 29 July 2024

References

- Holford M, Daly M, King GF, Norton RS. Venoms to the rescue. *Science*. 2018;361(6405):842–4. Available from: <http://eutils.ncbi.nlm.nih.gov/entrez/eutils/elink.fcgi?dbfrom=pubmed&id=30166472&retmode=ref&cmd=prlinks>.
- von Reumont BM, Anderlüh G, Antunes A, Ayvazyan N, Beis D, Caliskan F, et al. Modern venomomics—current insights, novel methods, and future perspectives in biological and applied animal venom research. *GigaScience*. 2022;11:1–27. <https://doi.org/10.1093/gigascience/giac048>.
- King GF. Tying pest insects in knots: the deployment of spider-venom-derived knottins as bioinsecticides. *Pest Manag Sci*. 2019;75(9):2437–45. Available from: <https://onlinelibrary.wiley.com/doi/abs/10.1002/ps.5452>.
- King G. *Venoms to Drugs*. Cambridge, UK: Royal Society of Chemistry; 2015. (Venom as a Source for the Development of Human Therapeutics). Available from: http://books.google.de/books?id=Gb-ZBgAAQBAJ&printsec=frontcover&dq=Venoms+to+Drugs&hl=&cd=1&source=gbs_api.
- de Castro Figueiredo Bordon K, Cologna CT, Fornari-Baldo EC, Pinheiro-Júnior EL, Cerni FA, Amorim FG, et al. From animal poisons and venoms to medicines: achievements, challenges and perspectives in drug

- discovery. *Front Pharmacol.* 2020;11(1132):1–29. Available from: <https://www.frontiersin.org/articles/10.3389/fphar.2020.01132>.
6. von Reumont BM, Campbell LI, Jenner RA. *Quo vadis venomics?* A road-map to neglected venomous invertebrates. *Toxins.* 2014;6(12):3488–551. Available from: <http://eutils.ncbi.nlm.nih.gov/entrez/eutils/elink.fcgi?dbfrom=pubmed&id=25533518&retmode=ref&cmd=prlinks>.
 7. Walker AA, Robinson SD, Yeates DK, Jin J, Baumann K, Dobson J, et al. Entomo-venomics—the evolution, biology and biochemistry of insect venoms. *Toxicon.* 2018;154:15–27. <https://doi.org/10.1016/j.toxicon.2018.09.004>.
 8. Lüddecke T, Herzog V, von Reumont BM, Vilcinskas A. The biology and evolution of spider venoms. *Biol Rev Camb Philos Soc.* 2022;97(1):163–78.
 9. Harris RJ, Jenner RA. Evolutionary ecology of fish venom: adaptations and consequences of evolving a venom system. *Toxins.* 2019;11(2):60. Available from: <http://www.mdpi.com/2072-6651/11/2/60>.
 10. von Reumont BM, Campbell LI, Richter S, Hering L, Sykes D, Hetmank J, et al. A polychaete's powerful punch: venom gland transcriptomics of *Glycera* reveals a complex cocktail of toxin homologs. *Genome Biol Evol.* 2014;6(9):2406–23. Available from: <http://eutils.ncbi.nlm.nih.gov/entrez/eutils/elink.fcgi?dbfrom=pubmed&id=25193302&retmode=ref&cmd=prlinks>.
 11. Richter S, Helm C, Meunier FA, Hering L, Campbell LI, Drukewitz SH, et al. Comparative analyses of glycerotoxin expression unveil a novel structural organization of the bloodworm venom system. *BMC Evol Biol.* 2017;17(1):64. Available from: <http://bmcevolbiol.biomedcentral.com/articles/10.1186/s12862-017-0904-4>.
 12. von Reumont BM, Lüddecke T, Timm T, Lochnit G, Vilcinskas A, von Döhren J, et al. Proteo-transcriptomic analysis identifies potential novel toxins secreted by the predatory, prey-piercing ribbon worm *Amphiporus lactifloreus*. *Mar Drugs.* 2020;18(8):407. Available from: <https://www.mdpi.com/1660-3397/18/8/407>.
 13. Sachkova MY, Singer SA, Macrander J, Reitzel AM, Peigneur S, Tytgat J, et al. The birth and death of toxins with distinct functions: a case study in the sea anemone *Nematostella*. *Mol Biol Evol.* 2019;36(9):2001–12. Available from: <https://academic.oup.com/mbe/article/36/9/2001/5499077>.
 14. AmreenNisa S, Vinu D, Krupakar P, Govindaraju K, Sharma D, Vivek R. Jellyfish venom proteins and their pharmacological potentials: a review. *Int J Biol Macromol.* 2021;176:424–36. Available from: <https://www.sciencedirect.com/science/article/pii/S0141813021003548>.
 15. Lau MT, Manion J, Littleboy JB, Oyston L, Khuong TM, Wang QP, et al. Molecular dissection of box jellyfish venom cytotoxicity highlights an effective venom antidote. *Nat Commun.* 2019;10(1):1655. Available from: <https://www.nature.com/articles/s41467-019-09681-1>.
 16. Verdes A, Taboada S, Hamilton BR, Undheim EAB, Sonoda GG, Andrade SCS, et al. Evolution, expression patterns, and distribution of novel ribbon worm predatory and defensive toxins. *Mol Biol Evol.* 2022;39(5):msac096. <https://doi.org/10.1093/molbev/msac096>.
 17. Whitelaw BL, Cooke IR, Finn J, da Fonseca RR, Ritschard EA, Gilbert MTP, et al. Adaptive venom evolution and toxicity in octopods is driven by extensive novel gene formation, expansion, and loss. *GigaScience.* 2020;9(11). Available from: <https://academic.oup.com/gigasience/article/9/11/giaa120/5974087>.
 18. Whitelaw BL, Strugnell JM, Faou P, da Fonseca RR, Hall NE, Norman M, et al. Combined transcriptomic and proteomic analysis of the posterior salivary gland from the southern blue-ringed octopus and the southern sand octopus. *J Proteome Res.* 2016;15(9):3284–97. Available from: <http://eutils.ncbi.nlm.nih.gov/entrez/eutils/elink.fcgi?dbfrom=pubmed&id=27427999&retmode=ref&cmd=prlinks>.
 19. Dutertre S, Jin AH, Vetter I, Hamilton B, Sunagar K, Lavergne V, et al. Evolution of separate predation- and defence-evoked venoms in carnivorous cone snails. *Nat Commun.* 2014;5(3521):1–9. Available from: <http://eutils.ncbi.nlm.nih.gov/entrez/eutils/elink.fcgi?dbfrom=pubmed&id=24662800&retmode=ref&cmd=prlinks>.
 20. Schendel, Rash, Jenner, Undheim. The diversity of venom: the importance of behavior and venom system morphology in understanding its ecology and evolution. *Toxins.* 2019;11(11):666.
 21. Casewell NR, Wüster W, Vonk FJ, Harrison RA, Fry BG. Complex cocktails: the evolutionary novelty of venoms. *Trends Ecol Evol.* 2013;28(4):219–29. Available from: <http://eutils.ncbi.nlm.nih.gov/entrez/eutils/elink.fcgi?dbfrom=pubmed&id=23219381&retmode=ref&cmd=prlinks>.
 22. Drukewitz SH, von Reumont BM. The significance of comparative genomics in modern evolutionary venomics. *Front Ecol Evol.* 2019;7:163. Available from: <https://www.frontiersin.org/article/10.3389/fevo.2019.00163/full>.
 23. Koludarov I, Velasque M, Senoner T, Timm T, Greve C, Hamadou AB, et al. Prevalent bee venom genes evolved before the aculeate stinger and eusociality. *BMC Biol.* 2023;21(1):229. <https://doi.org/10.1186/s12915-023-01656-5>.
 24. Jackson TNW, Koludarov I. How the toxin got its toxicity. *Front Pharmacol.* 2020;11:1893. Available from: <https://www.frontiersin.org/article/10.3389/fphar.2020.574925>.
 25. Zancolli G, Casewell NR. Venom systems as models for studying the origin and regulation of evolutionary novelties. Kelley J, editor. *Mol Biol Evol.* 2020;37(10):2777–90. Available from: <https://academic.oup.com/mbe/article/37/10/2777/5848011>.
 26. von Reumont BM, Blanke A, Richter S, Alvarez F, Bleidorn C, Jenner RA. The first venomous crustacean revealed by transcriptomics and functional morphology: remipedee venom glands express a unique toxin cocktail dominated by enzymes and a neurotoxin. *Mol Biol Evol.* 2014;31(1):48–58. Available from: <http://eutils.ncbi.nlm.nih.gov/entrez/eutils/elink.fcgi?dbfrom=pubmed&id=24132120&retmode=ref&cmd=prlinks>.
 27. von Reumont BM, Undheim EAB, Jauss RT, Jenner RA. Venomics of remipedee crustaceans reveals novel peptide diversity and illuminates the venom's biological role. *Toxins.* 2017;9(8):1–25. Available from: <http://eutils.ncbi.nlm.nih.gov/entrez/eutils/elink.fcgi?dbfrom=pubmed&id=28933727&retmode=ref&cmd=prlinks>.
 28. Yager J. Remipedia, a new class of Crustacea from a marine cave in the Bahamas. *J Crustac Biol.* 1981;1(3):328–33. Available from: <http://www.jstor.org/stable/1547965>.
 29. Olesen J, Meland K, Glenner H, Hengstum PJV, Iliffe TM. *Xibalbanus cozumelensis*, a new species of Remipedia (Crustacea) from Cozumel, Mexico, and a molecular phylogeny of Xibalbanus on the Yucatán Peninsula. *Eur J Taxon.* 2017;316:1–27. Available from: <https://eurjournaloftaxonomy.eu/index.php/ejt/article/view/441>.
 30. Ertaş B, von Reumont BM, Wagele JW, Misof B, Burmester T. Hemocyanin suggests a close relationship of remipedia and hexapoda. *Mol Biol Evol.* 2009;26(12):2711–8. <https://academic.oup.com/mbe/article-lookup/doi/10.1093/molbev/msp186>.
 31. von Reumont BM, Jenner RA, Wills MA, Dell'Ampio E, Pass G, Ebersberger I, et al. Pancrustacean phylogeny in the light of new phylogenomic data: support for Remipedia as the possible sister group of Hexapoda. *Mol Biol Evol.* 2012;29(3):1031–45. Available from: <http://eutils.ncbi.nlm.nih.gov/entrez/eutils/elink.fcgi?dbfrom=pubmed&id=22049065&retmode=ref&cmd=prlinks>.
 32. Misof B, Liu S, Meusemann K, Peters RS, Donath A, Mayer C, et al. Phylogenomics resolves the timing and pattern of insect evolution. *Science.* 2014;346(6210):763–7. Available from: <http://eutils.ncbi.nlm.nih.gov/entrez/eutils/elink.fcgi?dbfrom=pubmed&id=25378627&retmode=ref&cmd=prlinks>.
 33. Lozano-Fernandez J, Giacomelli M, Fleming JF, Chen A, Vinther J, Thomsen PF, et al. Pancrustacean evolution illuminated by taxon-rich genomic-scale data sets with an expanded remipedee sampling. *Genome Biol Evol.* 2019;11(8):2055–70. Available from: <https://academic.oup.com/gbe/article/11/8/2055/5528088>.
 34. Bernot JP, Owen CL, Wolfe JM, Meland K, Olesen J, Crandall KA. Major revisions in pancrustacean phylogeny and evidence of sensitivity to taxon sampling. *Mol Biol Evol.* 2023;40(8):msad175. <https://doi.org/10.1093/molbev/msad175>.
 35. Neiber MT, Hartke TR, Stemme T, Bergmann A, Rust J, Iliffe TM, et al. Global biodiversity and phylogenetic evaluation of Remipedia (Crustacea). *PLoS One.* 2011;6(5):e19627. Available from: <http://dx.plos.org/10.1371/journal.pone.0019627.t001>.
 36. van der Ham JL, Felgenhauer BE. The functional morphology of the putative injecting apparatus of *Speleonectes tanumekes* (Remipedia). *J Crustac Biol.* 2007;27(1):1–9. Available from: <http://www.bioone.org/doi/abs/10.1651/S-2778.1>.

37. Postic G, Gracy J, Perin C, Chiche L, Gelly JC. KNOTTIN: the database of inhibitor cystine knot scaffold after 10 years, toward a systematic structure modeling. *Nucleic Acids Res.* 2018;46(1):454–8. Available from: <http://eutils.ncbi.nlm.nih.gov/entrez/eutils/elink.fcgi?dbfrom=pubmed&id=29136213&retmode=ref&cmd=prlinks>.
38. Pallaghy PK, Nielsen KJ, Craik DJ. A common structural motif incorporating a cystine knot and a triple-stranded β -sheetin toxic and inhibitory polypeptides. *Protein Sci.* 1994;3:1833–9.
39. Moore SJ, Leung CL, Cochran JR. Knottins: disulfide-bonded therapeutic and diagnostic peptides. *Drug Discov Today Technol.* 2012;9(1):1833–9. <https://doi.org/10.1016/j.ddtec.2011.07.003>.
40. Schwentner M, Combosch DJ, Pakes Nelson J, Giribet G. A phylogenomic solution to the origin of insects by resolving crustacean-hexapod relationships. *Curr Biol CB.* 2017;27(12):1818–24. Available from: <http://eutils.ncbi.nlm.nih.gov/entrez/eutils/elink.fcgi?dbfrom=pubmed&id=28602656&retmode=ref&cmd=prlinks>.
41. Ozbek R, Wielsch N, Vogel H, Lochnit G, Foerster F, Vilcinskis A, et al. Proteo-transcriptomic characterization of the venom from the endoparasitoid wasp *Pimpla turionellae* with aspects on its biology and evolution. *Toxins.* 2019;11(12):721.
42. van Cann M, Kuzmenkov A, Isensee J, Andreev-Andrievskiy A, Peigneur S, Khusainov G, et al. Scorpion toxin MeuNaTx α -1 sensitizes primary nociceptors by selective modulation of voltage-gated sodium channels. *FEBS J.* 2021;288(7):2418–35. Available from: <https://onlinelibrary.wiley.com/doi/abs/10.1111/febs.15593>.
43. Siemens J, Zhou S, Piskorowski R, Nikai T, Lumpkin EA, Basbaum AI, et al. Spider toxins activate the capsaicin receptor to produce inflammatory pain. *Nature.* 2006;444(7116):208–12.
44. Rodríguez AA, Salceda E, Garateix AG, Zaharenko AJ, Peigneur S, López O, et al. A novel sea anemone peptide that inhibits acid-sensing ion channels. *Peptides.* 2014;53:3–12.
45. Isensee J, Wenzel C, Buschow R, Weissmann R, Kuss AW, Hucho T. Subgroup-elimination transcriptomics identifies signaling proteins that define subclasses of TRPV1-positive neurons and a novel paracrine circuit. *PLoS One.* 2014;9(12):e115731.
46. Isensee J, Diskar M, Waldherr S, Buschow R, Hasenauer J, Prinz A, et al. Pain modulators regulate the dynamics of PKA-RII phosphorylation in subgroups of sensory neurons. *J Cell Sci.* 2014;127(1):216–29. Available from: <http://jcs.biologists.org/cgi/doi/10.1242/jcs.136580>.
47. Isensee J, Krahé L, Moeller K, Pereira V, Sexton JE, Sun X, et al. Syn-ergistic regulation of serotonin and opioid signaling contributes to pain insensitivity in Nav1.7 knockout mice. *Sci Signal.* 2017;10(461):1–27. Available from: <https://stke.sciencemag.org/content/10/461/eaah4874>.
48. Isensee J, van Cann M, Despang P, Araldi D, Moeller K, Petersen J, et al. Depolarization induces nociceptor sensitization by CaV β 12-mediated PKA-II activation. *J Cell Biol.* 2021;220(10):e202002083. Available from: <https://www.ncbi.nlm.nih.gov/pmc/articles/PMC8404467/>.
49. Isensee J, Kaufholz M, Knappe MJ, Hasenauer J, Hammerich H, Gonzalez-Jorge H, et al. PKA-RII subunit phosphorylation precedes activation by cAMP and regulates activity termination. *J Cell Biol.* 2018;217(6):2167–84. Available from: <https://rupress.org/jcb/article/217/6/2167/39303/PKARII-subunit-phosphorylation-precedes-activation>.
50. Garza Carbajal A, Ebersberger A, Thiel A, Ferrari L, Acuna J, Brosig S, et al. Oncostatin M induces hyperalgesic priming and amplifies signaling of cAMP to ERK by RapGEF2 and PKA. *J Neurochem.* 2021;157(6):1821–37.
51. Rubinfeld H, Seger R. The ERK cascade: a prototype of MAPK signaling. *Mol Biotechnol.* 2005;31(2):151–74.
52. Murphy LO, Blenis J. MAPK signal specificity: the right place at the right time. *Trends Biochem Sci.* 2006;31(5):268–75. Available from: [https://www.cell.com/trends/biochemical-sciences/abstract/S0968-0004\(06\)00086-7](https://www.cell.com/trends/biochemical-sciences/abstract/S0968-0004(06)00086-7).
53. Skyba DA, Radhakrishnan R, Bement MKH, Sluka KA. The cAMP pathway and pain: potential targets for drug development. *Drug Discov Today Dis Models.* 2004;1(2):115–9. Available from: <https://www.sciencedirect.com/science/article/pii/S1740675704000131>.
54. Zhang X, Li F, Guo L, Hei H, Tian L, Peng W, et al. Forskolin regulates L-type calcium channel through interaction between actinin 4 and β 3 subunit in osteoblasts. *PLoS One.* 2015;10(4):e0124274.
55. Cury Y, Picolo G, Gutierrez VP, Ferreira SH. Pain and analgesia: The dual effect of nitric oxide in the nociceptive system. *Nitric Oxide.* 2011;25(3):243–54. Available from: <https://www.sciencedirect.com/science/article/pii/S1089860311004344>.
56. Maxwell MJ, Thekkadam C, Lamboley C, Chin YKY, Crawford T, Smith JJ, et al. A bivalent remipede toxin promotes calcium release via ryanodine receptor activation. *Nat Commun.* 2023;14(1036):1–13. Available from: <https://www.nature.com/articles/s41467-023-36579-w>.
57. ProtTrans: Toward understanding the language of life through self-supervised learning. Available from: <https://www.computer.org/csdl/journal/tp/2022/10/09477085/1v2M3TwoN4A>. Cited 2024 Apr 29.
58. Jin L, Fang M, Chen M, Zhou C, Ombati R, Hakim MA, et al. An insecticidal toxin from *Nephila clavata* spider venom. *Amino Acids.* 2017;49(7):1237–45. Available from: <http://eutils.ncbi.nlm.nih.gov/entrez/eutils/elink.fcgi?dbfrom=pubmed&id=28497266&retmode=ref&cmd=prlinks>.
59. Kalina RS, Kasheverov IE, Koshelev SG, Sintsova OV, Peigneur S, Pinheiro-Junior EL, et al. Nicotinic acetylcholine receptors are novel targets of APETx-like toxins from the sea anemone *Heteractis magnifica*. *Toxins.* 2022;14(10):697.
60. Pinheiro-Junior EL, Kalina R, Gladkikh I, Leychenko E, Tytgat J, Peigneur S. A tale of toxin promiscuity: the versatile pharmacological effects of Hcr 1b-2 sea anemone peptide on voltage-gated ion channels. *Mar Drugs.* 2022;20(2):147.
61. D'Adamo MC, Liantonio A, Rolland JF, Pessia M, Imbrici P, Kv1.1 Channelopathies: pathophysiological mechanisms and therapeutic approaches. *Int J Mol Sci.* 2020;21(8):2935. Available from: <https://www.ncbi.nlm.nih.gov/pmc/articles/PMC7215777/>.
62. Kuzmenkov AI, Vassilevski AA, Kudryashova KS, Nekrasova OV, Peigneur S, Tytgat J, et al. Variability of potassium channel blockers in Mesobuthus eupeus scorpion venom with focus on Kv1.1. *J Biol Chem.* 2015;290(19):12195–209. Available from: <https://www.ncbi.nlm.nih.gov/pmc/articles/PMC4424352/>.
63. Beraud E, Viola A, Regaya I, Confort-Gouny S, Siaud P, Ibarrola D, et al. Block of neural Kv1.1 potassium channels for neuroinflammatory disease therapy. *Ann Neurol.* 2006;60(5):586–96.
64. Nekrasova OV, Volyntseva AD, Kudryashova KS, Novoseletsky VN, Lyapina EA, Illarionova AV, et al. Complexes of peptide blockers with Kv1.6 pore domain: molecular modeling and studies with KcsA-Kv1.6 channel. *J Neuroimmune Pharmacol.* 2017;12(2):260–76. <https://doi.org/10.1007/s11481-016-9710-9>.
65. Kimura T. Stability and safety of inhibitor cystine knot peptide, Gtx1–15, from the tarantula spider *Grammostola rosea*. *Toxins.* 2021;13(9):621. Available from: <https://www.mdpi.com/2072-6651/13/9/621>.
66. Thouta S, Zhang Y, Garcia E, Snutch TP. Kv1.1 channels mediate network excitability and feed-forward inhibition in local amygdala circuits. *Sci Rep.* 2021;11(15180). Available from: <https://www.ncbi.nlm.nih.gov/pmc/articles/PMC8313690/>.
67. Ushkaryov YA, Rohou A, Sugita S. α -Latrotoxin and its receptors. *Handb Exp Pharmacol.* 2008;184:171–206. Available from: <https://www.ncbi.nlm.nih.gov/pmc/articles/PMC2519134/>.
68. Taiwo YO, Levine JD. Further confirmation of the role of adenylyl cyclase and of cAMP-dependent protein kinase in primary afferent hyperalgesia. *Neuroscience.* 1991;44(1):131–5.
69. Pitchford S, Levine JD. Prostaglandins sensitize nociceptors in cell culture. *Neurosci Lett.* 1991;132(1):105–8.
70. Kress M, Rödl J, Reeh PW. Stable analogues of cyclic AMP but not cyclic GMP sensitize unmyelinated primary afferents in rat skin to heat stimulation but not to inflammatory mediators, *in vitro*. *Neuroscience.* 1996;74(2):609–17.
71. Bao Y, Gao Y, Yang L, Kong X, Zheng H, Hou W, et al. New insights into protease-activated receptor 4 signaling pathways in the pathogenesis of inflammation and neuropathic pain: a literature review. *Channels.* 2015;9(1):5–13. Available from: <https://www.ncbi.nlm.nih.gov/pmc/articles/PMC4594588/>.
72. Krishnan A, Almén MS, Fredriksson R, Schiöth HB. The origin of GPCRs: identification of mammalian like Rhodopsin, Adhesion, Glutamate and Fizzled GPCRs in fungi. *PLoS One.* 2012;7(1):e29817. Available from: <https://www.frontiersin.org/journals/physiology/articles/10.3389/fphys.2018.01049/full>.

73. Manning G, Young SL, Miller WT, Zhai Y. The protist, *Monosiga brevicollis*, has a tyrosine kinase signaling network more elaborate and diverse than found in any known metazoan. *Proc Natl Acad Sci U S A*. 2008;105(28):9674–9.
74. Walters ET. Nociceptive biology of molluscs and arthropods: evolutionary clues about functions and mechanisms potentially related to pain. *Front Physiol*. 2018;9. Available from: <https://www.frontiersin.org/journals/physiology/articles/10.3389/fphys.2018.01049/full>.
75. Chin J, Liu RY, Cleary LJ, Eskin A, Byrne JH. TGF-beta1-induced long-term changes in neuronal excitability in aplysia sensory neurons depend on MAPK. *J Neurophysiol*. 2006;95(5):3286–90.
76. Liao X, Gunstream JD, Lewin MR, Ambron RT, Walters ET. Activation of protein kinase A contributes to the expression but not the induction of long-term hyperexcitability caused by axotomy of *Aplysia* sensory neurons. *J Neurosci Off J Soc Neurosci*. 1999;19(4):1247–56.
77. Walters ET. Nociceptive biology of molluscs and arthropods: evolutionary clues about functions and mechanisms potentially related to pain. *Front Physiol*. 2018;9(1049):1–22.
78. Walters ET. Exaptation and evolutionary adaptation in nociceptor mechanisms driving persistent pain. *Brain Behav Evol*. 2023;98(6):314–30. <https://doi.org/10.1159/000535552>.
79. Walters ET, Crook RJ, Neely GG, Price TJ, Smith ESJ. Persistent nociceptor hyperactivity as a painful evolutionary adaptation. *Trends Neurosci*. 2023;46(3):211–27. Available from: <https://linkinghub.elsevier.com/retrieve/pii/S0166223622002612>.
80. Dowell NL, Giorgianni MW, Kassner VA, Selegue JE. The deep origin and recent loss of venom toxin genes in rattlesnakes. *Curr Biol*. 2016;26(18):2434–45. Available from: <http://eutils.ncbi.nlm.nih.gov/entrez/eutils/elink.fcgi?dbfrom=pubmed&id=27641771&retmode=ref&cmd=prlinks>.
81. Koludarov I, Senoner T, Jackson TNW, Dashevsky D, Heinzinger M, Aird SD, et al. Domain loss enabled evolution of novel functions in the snake three-finger toxin gene superfamily. *Nat Commun*. 2023;14(1):4861. Available from: <https://www.nature.com/articles/s41467-023-40550-0>.
82. Drukewitz SH, Bokelmann L, Undheim EAB, von Reumont BM. Toxins from scratch? Diverse, multimodal gene origins in the predatory robber fly *Dasygogon diadema* indicate a dynamic venom evolution in dipteran insects. *GigaScience*. 2019;8(7):1–13. Available from: <https://academic.oup.com/gigascience/article/doi/10.1093/gigascience/giz081/5530325>.
83. Barua A, Koludarov I, Mikheyev AS. Co-option of the same ancestral gene family gave rise to mammalian and reptilian toxins. *BMC Biol*. 2021;19(1):268. <https://doi.org/10.1186/s12915-021-01191-1>.
84. Jenner RA. Sequence alignments (from Supplementary data remipede Toxins paper), von Reumont et al. Data set resource. Natural History Museum.; 2017. Available from: <https://data.nhm.ac.uk/dataset/supplementary-data-remipede-toxins-paper/resource/45bb9a03-3a84-4c98-88b5-9b811dddc733>.
85. Billen B, Vassilevski A, Nikolsky A, Debaveye S, Tytgat J, Grishin E. Unique bell-shaped voltage-dependent modulation of Na⁺ channel gating by novel insect-selective toxins from the spider *Agelena orientalis*. *J Biol Chem*. 2010;285(24):18545–54. Available from: <http://eutils.ncbi.nlm.nih.gov/entrez/eutils/elink.fcgi?dbfrom=pubmed&id=20385552&retmode=ref&cmd=prlinks>.
86. Deutsch EW, Bandeira N, Sharma V, Perez-Riverol Y, Carver JJ, Kundu DJ, et al. The ProteomeXchange consortium in 2020: enabling 'big data' approaches in proteomics. *Nucleic Acids Res*. 2020;48(D1):D1145–52. <https://doi.org/10.1093/nar/gkz984>. Cited 2023 Apr 2.
87. Hempel BF. Non-cytotoxic xibalbin ICK variants from remipede crustaceans. *MassIVE*; Available from: <https://massive.ucsd.edu/ProteoSAFe/dataset.jsp?task=058eae6afbb5402a987e9ca55312f8cc>.
88. Zhou X, Guo G, Yu S, Hu R. MiR-21–5p alleviates trigeminal neuralgia in rats through down-regulation of voltage-gated potassium channel Kv1.1. *Zhong Nan Da Xue Xue Bao Yi Xue Ban*. 2024;49(1):29–39.
89. Zhou, X. *Rattus norvegicus* potassium voltage-gated channel subfamily A member 1 (Kcna1), mRNA. GenBank. Available from: https://www.ncbi.nlm.nih.gov/nucleotide/NM_173095.
90. Peng Y. *Rattus norvegicus* potassium voltage-gated channel subfamily A member 2 (Kcna2), mRNA. GenBank. Available from: https://www.ncbi.nlm.nih.gov/nucleotide/NM_012970.
91. Peng Y, Zhang Q, Cheng H, Yan G, Xing C. Upregulation of ubiquitin conjugating enzyme E2B (Ube2b) ameliorates neuropathic pain by regulating Kcna2 (potassium voltage-gated channel subfamily A member 2) in primary afferent neurons. *Bioengineered*. 2021;12(1):7470–80.
92. Soldovieri M. *Homo sapiens* potassium voltage-gated channel subfamily A member 3 (KCNA3), transcript variant 1, mRNA. GenBank. Available from: https://www.ncbi.nlm.nih.gov/nucleotide/NM_002232.
93. Generalovic TN, McCarthy SA, Warren IA, Wood JMD, Torrance J, Sims Y, et al. A high-quality, chromosome-level genome assembly of the Black Soldier Fly (*Hermetia illucens* L.). *Sethuraman A, editor. G3 GenesGenomesGenetics*. 2021;11(5):jkab085. Available from: <https://academic.oup.com/g3journal/article/doi/10.1093/g3journal/jkab085/6178282>.
94. O'Donovan B. *Rattus norvegicus* potassium voltage-gated channel subfamily A member 4 (Kcna4), mRNA. GenBank. Available from: https://www.ncbi.nlm.nih.gov/nucleotide/NM_012971.
95. O'Donovan B, Adeluyi A, Anderson EL, Cole RD, Turner JR, Ortinski PI. Altered gating of Kv1.4 in the nucleus accumbens suppresses motivation for reward. *eLife*. 2019;8:e47870.
96. Zhu J. *Rattus norvegicus* potassium voltage-gated channel subfamily A member 6 (Kcna6), mRNA. GenBank. Available from: https://www.ncbi.nlm.nih.gov/nucleotide/NM_023954.
97. Zhu J, Yan J, Thornhill WB. The Kv1.3 potassium channel is localized to the cis-Golgi and Kv1.6 is localized to the endoplasmic reticulum in rat astrocytes. *FEBS J*. 2014;281(15):3433–45.
98. Fernandez-Marino A. *Homo sapiens* potassium voltage-gated channel subfamily B member 1 (KCNB1), mRNA. GenBank. Available from: https://www.ncbi.nlm.nih.gov/nucleotide/NM_004975.
99. Fernández-Mariño AI, Tan XF, Bae C, Huffer K, Jiang J, Swartz KJ. Inactivation of the Kv2.1 channel through electromechanical coupling. *Nature*. 2023;622(7982):410–7.
100. Clatot J. *Homo sapiens* potassium voltage-gated channel subfamily C member 1 (KCNK1), transcript variant 2, mRNA. GenBank. Available from: https://www.ncbi.nlm.nih.gov/nucleotide/NM_004976.
101. Clatot J, Ginn N, Costain G, Goldberg EM. A KCNC1-related neurological disorder due to gain of Kv3.1 function. *Ann Clin Transl Neurol*. 2023;10(1):111–7.
102. Kanda H, Ling J, Chang YT, Erol F, Viatchenko-Karpinski V, Yamada A, et al. Kv4.3 channel dysfunction contributes to trigeminal neuropathic pain manifested with orofacial cold hypersensitivity in rats. *J Neurosci Off J Soc Neurosci*. 2021;41(10):2091–105.
103. Kanda H. *Rattus norvegicus* potassium voltage-gated channel subfamily D member 3 (Kcnd3), transcript variant 3, mRNA. GenBank. Available from: https://www.ncbi.nlm.nih.gov/nucleotide/NM_031739.
104. Tian MQ, Li RK, Yang F, Shu XM, Li J, Chen J, et al. Phenotypic expansion of KCNH1-associated disorders to include isolated epilepsy and its associations with genotypes and molecular sub-regional locations. *CNS Neurosci Ther*. 2023;29(1):270–81.
105. Tian M. *Homo sapiens* potassium voltage-gated channel subfamily H member 1 (KCNH1), transcript variant 1, mRNA. GenBank. Available from: https://www.ncbi.nlm.nih.gov/nucleotide/NM_172362.
106. Thomson K. *Homo sapiens* potassium voltage-gated channel subfamily H member 2 (KCNH2), transcript variant 1, mRNA. GenBank. Available from: https://www.ncbi.nlm.nih.gov/nucleotide/NM_000238.
107. Thomson KL, Jiang C, Richardson E, Westphal DS, Burkard T, Wolf CM, et al. Clinical interpretation of KCNH2 variants using a robust PS3/BS3 functional patch-clamp assay. *HGG Adv*. 2024;5(2):100270.
108. Matthews B. *Drosophila melanogaster* shaker, transcript variant E (Sh), mRNA. GenBank. Available from: https://www.ncbi.nlm.nih.gov/nucleotide/NM_167595.
109. Matthews BB, Dos Santos G, Crosby MA, Emmert DB, St Pierre SE, Gramates LS, et al. Gene model annotations for *Drosophila melanogaster*: impact of high-throughput data. *G3 Bethesda Md*. 2015;5(8):1721–36.
110. van Cann M. *Rattus norvegicus* sodium voltage-gated channel alpha subunit 2 (Scn2a), mRNA. GenBank. Available from: https://www.ncbi.nlm.nih.gov/nucleotide/NM_012647.
111. Pan X. *Rattus norvegicus* sodium voltage-gated channel alpha subunit 4 (Scn4a), mRNA. GenBank. Available from: https://www.ncbi.nlm.nih.gov/nucleotide/NM_013178.
112. Pan X, Li Z, Zhou Q, Shen H, Wu K, Huang X, et al. Structure of the human voltage-gated sodium channel Nav1.4 in complex with β1. *eScience*. 2018;362(6412):eaa02486.

113. Shi J, Pan X, Wang Z, Yi M, Xie S, Zhang X, et al. SCN5A-L256del and L1621F exhibit loss-of-function properties related to autosomal recessive congenital cardiac disorders presenting as sick sinus syndrome, dilated cardiomyopathy, and sudden cardiac death. *Gene*. 2024;898:148093.
114. Shi J. *Homo sapiens* sodium voltage-gated channel alpha subunit 5 (SCN5A), transcript variant 1, mRNA. GeneBank. Available from: https://www.ncbi.nlm.nih.gov/nuccore/NM_198056.
115. King DR, Demirtas M, Tarasov M, Struckman HL, Meng X, Nassal D, et al. Cardiac-specific deletion of *scn8a* mitigates dravet syndrome-associated sudden death in adults. *JACC Clin Electrophysiol*. 2024;10(5):829–42.
116. King D. *Mus musculus* sodium channel, voltage-gated, type VIII, alpha (Scn8a), transcript variant 1, mRNA. GeneBank. Available from: https://www.ncbi.nlm.nih.gov/nuccore/NM_001077499.
117. Du Y. *Blattella germanica* sodium channel Nav (Nav) gene, partial cds. GeneBank. Available from: <https://www.ncbi.nlm.nih.gov/nuccore/DQ466887>.
118. Du Y, Nomura Y, Luo N, Liu Z, Lee JE, Khambay B, et al. Molecular determinants on the insect sodium channel for the specific action of type II pyrethroid insecticides. *Toxicol Appl Pharmacol*. 2009;234(2):266–72.
119. Al-Ward H. *Rattus norvegicus* sodium voltage-gated channel beta subunit 1 (Scn1b), transcript variant 1, mRNA. GeneBank. Available from: https://www.ncbi.nlm.nih.gov/nuccore/NM_001271045.
120. Al-Ward H, Liu N, Omorou M, Huang Y, Chen W, Liu CY, et al. The relationship between miRNA-210 and SCN1B in fetal rats with hypoxic-ischemic brain injury. *Biosci Rep*. 2023;43(1):BSR20222016.
121. Popa-Fotea N. *Homo sapiens* sodium voltage-gated channel beta subunit 1 (SCN1B), transcript variant a, mRNA. GeneBank. Available from: https://www.ncbi.nlm.nih.gov/nuccore/NM_001037.
122. Popa-Fotea NM, Oprescu N, Scafa-Udriste A, Micheu MM. Impact of rs1805127 and rs55742440 variants on atrial remodeling in hypertrophic cardiomyopathy patients with atrial fibrillation: a Romanian cohort study. *Int J Mol Sci*. 2023;24(24):17244.
123. Matthews B. *Drosophila melanogaster* temperature-induced paralytic E (tipE), transcript variant a, mRNA. GeneBank. Available from: https://www.ncbi.nlm.nih.gov/nuccore/NM_079196.
124. Cribbs L. *Rattus norvegicus* low voltage-activated, T-type calcium channel alpha subunit (CACNA1G) mRNA, complete cds. GenBank. Available from: <https://www.ncbi.nlm.nih.gov/nuccore/AF027984>.
125. Perez-Reyes E, Cribbs LL, Daud A, Lacerda AE, Barclay J, Williamson MP, et al. Molecular characterization of a neuronal low-voltage-activated T-type calcium channel. *Nature*. 1998;391(6670):896–900.
126. Cribbs LL, Lee JH, Yang J, Satin J, Zhang Y, Daud A, et al. Cloning and characterization of alpha1H from human heart, a member of the T-type Ca²⁺ channel gene family. *Circ Res*. 1998;83(1):103–9.
127. Cribbs LL. *Homo sapiens* T-type calcium channel alpha 1H subunit (CACNA1H) mRNA, complete cds. GeneBank. Available from: <https://www.ncbi.nlm.nih.gov/nuccore/AF051946>.
128. Lee J. *Rattus norvegicus* CACNA1I splicing variant c mRNA, partial cds; alternatively spliced. GeneBank; Available from: <https://www.ncbi.nlm.nih.gov/nuccore/AY128645>.
129. Lee JH, Daud AN, Cribbs LL, Lacerda AE, Pereverzev A, Klöckner U, et al. Cloning and expression of a novel member of the low voltage-activated T-type calcium channel family. *J Neurosci Off J Soc Neurosci*. 1999;19(6):1912–21.
130. Peigneur S, da Costa OC, de Sousa Fonseca FC, McMahon KL, Mueller A, Cheneval O, et al. Small cyclic sodium channel inhibitors. *Biochem Pharmacol*. 2021;183:114291.
131. von Reumont BM. Venom gland transcriptomics of *Xibalbanus tulumensis*. GeneBank; Available from: <https://www.ncbi.nlm.nih.gov/sra/SRX2766574>.
132. Schwentner, Marin. RNAseq of *Lasionectes entrichoma* using half head and some body segments. GeneBank; Available from: <https://www.ncbi.nlm.nih.gov/sra/SRX2085853>.
133. Lozano-Fernandez J. RNA-Seq of *Morlockia williamsi*. GeneBank. Available from: <https://www.ncbi.nlm.nih.gov/sra/?term=srr8280778>.
134. Lozano-Fernandez J. RNA-Seq of *Godzilliongnomus frondosus*. Available from: <https://www.ncbi.nlm.nih.gov/sra/?term=SRR8280777>.
135. Lozano-Fernandez J. RNA-Seq of *Pleomothra apletocheles*. Available from: <https://www.ncbi.nlm.nih.gov/sra/?term=SRR8280776>.
136. Andrews S. FastQC: a quality control tool for high throughput sequence data [Online]. Available from: Andrews, S. FastQC: A Quality Control Tool for High Throughput Sequence Data. 2010. Available online at: <http://www.bioinformatics.babraham.ac.uk/projects/fastqc/>.
137. Bolger AM, Lohse M, Usadel B. Trimmomatic: a flexible trimmer for Illumina sequence data. *Bioinformatics*. 2014;30(15):2114–20. Available from: <http://eutils.ncbi.nlm.nih.gov/entrez/eutils/elink.fcgi?dbfrom=pubmed&id=24695404&retmode=ref&cmd=prlinks>.
138. Grabherr MG, Haas BJ, Yassour M, Levin JZ, Thompson DA, Amit I, et al. Full-length transcriptome assembly from RNA-Seq data without a reference genome. *Nat Biotechnol*. 2011;29(7):644–52. Available from: <http://eutils.ncbi.nlm.nih.gov/entrez/eutils/elink.fcgi?dbfrom=pubmed&id=21572440&retmode=ref&cmd=prlinks>.
139. Haas BJ, Papanicolaou A, Yassour M, Grabherr M, Blood PD, Bowden J, et al. De novo transcript sequence reconstruction from RNA-seq using the Trinity platform for reference generation and analysis. *Nat Protoc*. 2013;8(8):1494–512. Available from: <http://www.nature.com/doi/10.1038/nprot.2013.084>.
140. Katoh K, Standley DM. MAFFT multiple sequence alignment software version 7: improvements in performance and usability. *Mol Biol Evol*. 2013;30(4):772–80. <https://doi.org/10.1093/molbev/mst010>.
141. Minh BQ, Schmidt HA, Chernomor O, Schrempf D, Woodhams MD, von Haeseler A, et al. IQ-TREE 2: new models and efficient methods for phylogenetic inference in the genomic era. *Mol Biol Evol*. 2020;37(5):1530–4. <https://doi.org/10.1093/molbev/msaa015>.
142. Hoang DT, Chernomor O, von Haeseler A, Minh BQ, Vinh LS. UFBoot2: improving the ultrafast bootstrap approximation. *Mol Biol Evol*. 2018;35(2):518–22. <https://doi.org/10.1093/molbev/msx281>.
143. Gabler F, Nam SZ, Till S, Mirdita M, Steinegger M, Söding J, et al. Protein sequence analysis using the MPI bioinformatics toolkit. *Curr Protoc Bioinformatics*. 2020;72(1):e108. Available from: <https://onlinelibrary.wiley.com/doi/abs/10.1002/cpbi.108>.
144. Ahmed Elnaggar, Michael Heinzinger, Christian Dallago, Ghalia Rehawi, Yu Wang, Llion Jones, Tom Gibbs, Tamas Feher, Christoph Angerer, Martin Steinegger, Debsindhu Bhowmik, Burkhard Rost. ProtTrans: Toward Understanding the Language of Life Through Self-Supervised Learning. *IEEE Trans Pattern Anal Mach Intell*. 2022;44(10):7112–27. <https://doi.org/10.1109/TPAMI.2021.3095381>.
145. Littmann M, Heinzinger M, Dallago C, Olenyi T, Rost B. Embeddings from deep learning transfer GO annotations beyond homology. *Sci Rep*. 2021;11(1):1160. Available from: <https://www.nature.com/articles/s41598-020-80786-0>.
146. von Reumont. Diversely evolved xibalbin variants from remipede venom inhibit potassium channels and activate PKA-II and Erk1/2 signaling. ZENODO; Available from: <https://zenodo.org/records/7808089>.

Publisher's Note

Springer Nature remains neutral with regard to jurisdictional claims in published maps and institutional affiliations.